

Ultra-Thin Lithium Silicide Interlayer for Solid-State Lithium-Metal Batteries

Jaekyung Sung, So Yeon Kim, Avetik Harutyunyan, Maedeh Amirmaleki, Yoonkwang Lee, Yeonguk Son, and Ju Li*

All-solid-state batteries with metallic lithium (Li_{BCC}) anode and solid electrolyte (SE) are under active development. However, an unstable SE/ Li_{BCC} interface due to electrochemical and mechanical instabilities hinders their operation. Herein, an ultra-thin nanoporous mixed ionic and electronic conductor (MIEC) interlayer ($\approx 3.25 \mu\text{m}$), which regulates Li_{BCC} deposition and stripping, serving as a 3D scaffold for Li^0 ad-atom formation, Li_{BCC} nucleation, and long-range transport of ions and electrons at SE/ Li_{BCC} interface is demonstrated. Consisting of lithium silicide and carbon nanotubes, the MIEC interlayer is thermodynamically stable against Li_{BCC} and highly lithiophilic. Moreover, its nanopores ($< 100 \text{ nm}$) confine the deposited Li_{BCC} to the size regime where Li_{BCC} exhibits “smaller is much softer” size-dependent plasticity governed by diffusive deformation mechanisms. The Li_{BCC} thus remains soft enough not to mechanically penetrate SE in contact. Upon further plating, Li_{BCC} grows in between the current collector and the MIEC interlayer, not directly contacting the SE. As a result, a full-cell having $\text{Li}_{3.75}\text{Si-CNT}/\text{Li}_{\text{BCC}}$ foil as an anode and $\text{LiNi}_{0.8}\text{Co}_{0.1}\text{Mn}_{0.1}\text{O}_2$ as a cathode displays a high specific capacity of 207.8 mAh g^{-1} , 92.0% initial Coulombic efficiency, 88.9% capacity retention after 200 cycles (Coulombic efficiency reaches 99.9% after tens of cycles), and excellent rate capability (76% at 5 C).

1. Introduction

The demand for safe rechargeable batteries with high energy density is ever-growing.^[1] To overcome the low theoretical capacity of graphite (372 mAh g^{-1}) in lithium-ion batteries (LIBs), attempts have been made to use metallic lithium in the body-centered cubic crystal (Li_{BCC}) phase as an anode material due to its high theoretical specific capacity (3860 mAh g^{-1}) and low reduction potential (-3.04 V vs standard hydrogen electrode).^[2] However, irregular growth of Li_{BCC} in the plating process can penetrate through the separator, bringing about short-circuiting and eventually fire and explosion.^[3] The use of liquid electrolytes with volatility and flammability aggravates safety concerns.^[4] Even if short-circuiting was no concern, low Coulombic efficiency limits the cyclability of the full-cell. This is probably related to not only side reactions at the Li_{BCC} /electrolyte contact during Li_{BCC}

deposition but also Li_{BCC} stripping-induced true-contact-area reduction that often becomes limiting kinetically. Since almost all Li^+ -conducting electrolytes are thermodynamically unstable when in contact with Li_{BCC} , the question is how to prevent the Li_{BCC} /electrolyte true contact area (and thus side reactions) from growing limitlessly (as in liquid electrolytes) while maintaining sufficient true contact area as well as connectivities for long-range ionic and electronic percolation. This is a key design problem that has to do with both stress and corrosion. Accordingly, all-solid-state battery (ASSB) configurations adopting solid electrolytes have been anticipated to be fundamentally different from liquid-electrolyte-based batteries in both the stress and corrosion aspects by virtue of their load-bearing capability and lack of fluidity. As such, the architectural design of ASSB is highly consequential.

Among a wide range of solid electrolytes (SEs), sulfide-based SEs have captivated researchers because it features high ionic conductivity of 10^{-2} to $10^{-4} \text{ S cm}^{-1}$ and mechanical ductility that enables the fabrication of densified electrodes on a large scale via a simple roll-to-roll slurry coating and calendaring process.^[5] That being said, argyrodite SE has severe intrinsic limitations from both thermodynamic and mechanical considerations. Thermodynamically, the reductive decomposition (side reaction) at the interface with Li_{BCC} (originating from its narrow electrochemical stability window^[6]) reduces the


J. Sung, S. Y. Kim, M. Amirmaleki, J. Li
Department of Nuclear Science and Engineering and Department
of Materials Science and Engineering
Massachusetts Institute of Technology
Cambridge, MA 02139, USA
E-mail: liju@mit.edu

J. Sung
Department of Materials Engineering and Convergence Technology
Gyeongsang National University
501 Jinju-daero, Jinju 52828, Republic of Korea

A. Harutyunyan
Honda Research Institute USA
San Jose, CA 95134, USA

Y. Lee
Advanced Battery Development Team
Hyundai Motor Company
Hwaseong 18280, Republic of Korea

Y. Son
Department of Chemical Engineering
Changwon National University
Changwon, Gyeongsangnam-do 51140, Republic of Korea

 The ORCID identification number(s) for the author(s) of this article can be found under <https://doi.org/10.1002/adma.202210835>.

© 2023 The Authors. Advanced Materials published by Wiley-VCH GmbH. This is an open access article under the terms of the Creative Commons Attribution License, which permits use, distribution and reproduction in any medium, provided the original work is properly cited.

DOI: 10.1002/adma.202210835

Coulombic efficiency of the full-cell. The formation of a series of by-products (Li_2S , Li_3P , and LiCl) with poorer ionic conductivity and their volumetric variation^[6b] can give rise to a large increase in impedance, especially if the interfacial area, when touched by Li_{BCC} , increases uncontrollably. Mechanically, small-scale Li_{BCC} can have hardness as high as tens of MPa, following the “smaller is stronger” trend of dislocation plasticity,^[7] and cause mechanical degradation of the SE. The local hardness can potentially be even higher when chemical impurities like S, P, and Cl, are mixed in, which can even turn the lithium metal (Li_{Metal}) amorphous.^[8] This means in electrodeposition, small size-confined Li_{Metal} (say a few hundred nanometers in diameter) can just displace and penetrate the soft argyrodite, like a hypodermic needle can penetrate the soft skin since, in deposition, a large mechanical pressure can be generated.^[9] Such high Li_{Metal} hardness-induced mechanical penetrations can increase the side-reaction area, thereby further reducing Coulombic efficiency and eventually resulting in internal short-circuiting. To address these concerns, various strategies, such as hybrid electrolytes^[10] ($\text{Li}_6\text{PS}_5\text{Cl}$ /poly(ethylene oxide) composite), alloys^[11] (In-Li and Ag-Li), and interlayers^[12] (e.g., polymer with Li salt, graphite, and Ag-C layer), have been proposed to “buffer” the direct contact of Li_{BCC} and SE. In particular, the Ag-C interlayer design developed by Lee et al.^[12e] manifested outstanding cycling stability with the aid of Ag, enabling the formation of dense Li_{BCC} at the interlayer’s interface with the current collector (CC) rather than the SE. Nevertheless, the use of costly noble metals is not desirable; thus, exploring the utilization of earth-abundant elements is necessary.

This exploration then calls for careful and fundamental considerations of the requirements that an interlayer for ASSB needs to meet. First, a material for the interlayer that is both thermodynamically and mechanically stable in contact with both Li_{BCC} and SE should be identified. An appropriate electrochemical stability window for the designed charging/discharging regimen is crucial; for lithium metal batteries, we are mainly interested in thermodynamic stability around ≈ 0 V versus Li^+/Li . In other words, the MIEC phase must be absolutely stable in naked contact with Li_{BCC} . On the phase diagram (could be binary, ternary, quaternary, etc.) containing Li element, material selection should be determined by the presence of a direct tie-line with the Li_{BCC} phase. The terminal lithiated phases of carbon, aluminum, silicon, etc., fit this requirement. Second, since the deposition/stripping generated cyclic stresses inside Li_{BCC} could fracture the interlayer or penetrate the SE, such stresses should be mitigated by the creeping of Li_{BCC} . For these reasons, we believe that an interlayer material should have properties of a mixed ionic and electronic conductor (MIEC) with a high surface area of 3D open porous structure and high lithiophilicity, thereby being capable of 1) nucleating Li_{BCC} homogeneously upon the initial lithiation and for later stripping/deposition; 2) offering high true contact area (i.e., numerous active sites) for charge-transfer reaction—faradaic reaction $\text{Li}^* \leftrightarrow \text{Li}^+ + \text{e}^-$, where Li^* is a surface ad-atom;^[13] and 3) maintaining long-range electronic/ionic percolations for high Li inventory reversibility during (de)lithiation^[9,14] (and significant Li ad-atom diffusivity, since Li ad-atom can be considered a composite of e^- and Li^+).

In particular, a length scale of ≤ 100 nm is desired for the pores of the MIEC interlayer. When a metal’s characteristic dimension is sufficiently confined to the nanoscale, the “smaller is stronger” trend of dislocation plasticity^[7] breaks down, and the metal falls into a “smaller is much weaker” regime governed by diffusion-enabled creep, as shown in Figure 1a. This suggests that the Li_{BCC} may behave like an “incompressible work fluid” during battery cycling.^[15] That is to say, nanosized pore confinement inside the 3D open-porous interlayer can drive the Li_{BCC} to “fluidize” sufficiently and reduce its plastic hardness $\ll 10$ MPa. This softening of the Li_{Metal} “hypodermic needle tip” would mitigate its penetration into the soft SE and also enable Li_{Metal} flow toward the reserved porosity. As such, both the SE and the interlayer can sustain less cyclic stress and retain their morphological integrity (Figure 1b).

Ideally, the working mechanism of the designed 3D open-porous MIEC interlayer will be as follows. Upon being intermeshed with the fluidized, tidal-wave-like Li_{BCC} on one end, and with the SE on another end, the interlayer would maintain long-range electronic and ionic contact. Specifically, the large internal surface areas of the open porous MIEC offer plenty of reaction area for the charge-transfer reaction $\text{Li}^*(\text{MIEC}) \leftrightarrow \text{Li}^+ + \text{e}^-$, where $\text{Li}^*(\text{MIEC})$ is an MIEC-surface-adsorbed Li ad-atom (Figure 1c) that is charge-neutral. Once the charge-transfer reaction is complete, the $\text{Li}^*(\text{MIEC})$ can diffuse on the inner surface of the open-porous MIEC and join the Li_{BCC} phases quite a long distance away, i.e., Li_{BCC} on the CC side as well as Li_{BCC} intermeshed inside the MIEC. This is similar to the daily routines of millions of people commuting on highways between the city center ($\text{Li}^*(\text{MIEC}@\text{SE})$) and sleeper-community suburbs ($\text{Li}_{\text{BCC}}(\text{MIEC}@\text{CC})$). The charge-transfer reaction $\text{Li}^*(\text{MIEC}@\text{SE}) \leftrightarrow \text{Li}^+ + \text{e}^-$ is analogous to a salaryman (Li^+) finding his car (e^-) near the city center, which can be a real headache but the open-porous MIEC provides plenty of parking spaces to accomplish this, as well a highway to the suburbs (Figure 1c).

Herein, we propose an open 3D nanoporous MIEC design of ultra-thin hybrid lithium silicide ($\text{Li}_{3.75}\text{Si}$)-carbon nanotubes (CNTs) interlayer (denoted as $\text{Li}_{3.75}\text{Si}$ -CNT) through the prelithiation of cheap silicon (Si). Figure 1d schematically illustrates the 3D MIEC interlayer design in this work, where the speculated pathways of Li^* formation and transport and Li_{BCC} phase nucleation and deformation/coarsening are identified in the designed configuration. Interestingly, the massive volume expansion of the Si host during the prelithiation, which was a well-known cause of capacity degradation in liquid-electrolyte-based LIBs,^[16] turned out to be beneficial in this work. This is because the expansion strain allows the formation of small-sized pores (< 100 nm) in between $\text{Li}_{3.75}\text{Si}$, and the soft metallic-alloy nature of $\text{Li}_{3.75}\text{Si}$ helps to consolidate the $\text{Li}_{3.75}\text{Si}$ particles (cold sintering) and improve the adhesion with SE. With this in situ consolidated and SE-adherent ultra-thin MIEC interlayer, we obtained stable reversible plating/stripping behavior on the stainless steel (SUS) CC in asymmetric solid-state cell configuration using sulfide-based argyrodite ($\text{Li}_6\text{PS}_5\text{Cl}$). A full-cell with NCM811 cathode achieved excellent cycling stability (97.65% after 49 cycles) at room temperature.

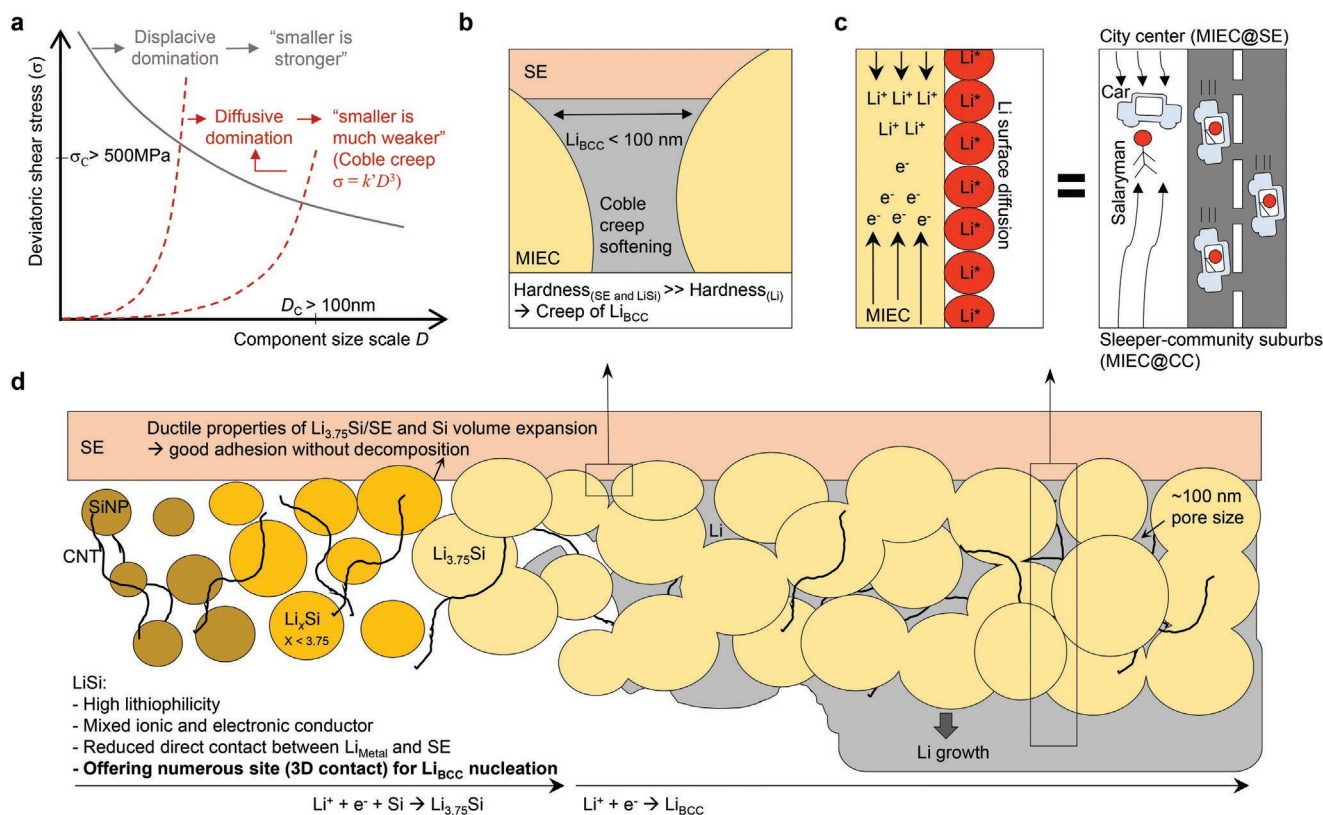


Figure 1. Li_{BCC} deposition mechanisms at $\text{Li}_{3.75}\text{Si}$ -CNT interlayer in ASSB. a) Semiquantitative illustration of the deformation mechanism map for metal (i.e., Sn).^[7] The gray curve denotes displacive deformation (Hall-Petch strengthening predicts the “smaller is stronger” trend). Surface diffusional deformation is governed by Coble creep. At a fixed strain rate, metal shows “smaller is weaker” (red curve). When reducing sample size, the competition between displacive deformation and diffusional deformation brings about a crossover which represents the transition between the two deformation mechanisms. b) Schematic showing porous MIEC structure having 100 nm Li_{BCC} within the pores, which indicates that softening of the Li_{Metal} prevents displacement and penetration of the soft SE and MIEC. c) Li_{BCC} deposition mechanism at interfaces (MIEC@SE and MIEC@CC) in porous MIEC interlayer. d) Schematic illustration (cross-section) of $\text{Li}_{3.75}\text{Si}$ -CNT interlayer in terms of Li_{BCC} deposition mechanism. Increase of state of charge (alloying reaction of Si, $x\text{Li}^+ + xe^- + \text{Si} \rightarrow \text{Li}_{3.75}\text{Si}$ and Li metal deposition, $\text{Li}^+ + e^- \rightarrow \text{Li}_{\text{BCC}}$) is shown to the right direction.

2. Results and Discussion

2.1. Fabrication of $\text{Li}_{3.75}\text{Si}$ -CNT Interlayer

We first prepared the commercial Si nanoparticles (SiNPs) with a particle size of $\approx 50\text{ nm}$, as shown in a scanning electron microscope (SEM) in Figure S1a in the Supporting Information. Transmission electron microscopy (TEM) image and its fast Fourier transform show a highly crystalline structure of Si nanoparticles (with 0.31 nm d -spacing for (111) plane) which coincides with X-ray diffraction (XRD) patterns (Figure S1b,c, Supporting Information). Then, a half-cell containing SiNP-CNT, $\text{Li}_6\text{PS}_5\text{Cl}$ as an SE separator, and Li_{BCC} foil as a counter-electrode was prepared for fabrication of the $\text{Li}_{3.75}\text{Si}$ -CNT interlayer (see details in the Experimental Section). Under a controlled external stack pressure, the prepared cell of SUS/SiNP-CNT/SE/ Li_{BCC} was discharged in constant current mode until the cut-off voltage of 5 mV was reached; the voltage profile is shown in Figure 2a. The cross-sectional SEM images of this cell displayed in Figure 2b–d and Figure S2 in the Supporting Information show that the SiNP-CNT layer with a thickness of $2\text{ }\mu\text{m}$ was transformed to the $\text{Li}_{3.75}\text{Si}$ -CNT layer with a thickness of $3.25\text{ }\mu\text{m}$ after the first discharging. Such

thin interlayer design is effective on increasing energy density of ASSB. Table S1 in the Supporting Information shows the comparison of $\text{Li}_{3.75}\text{Si}$ -CNT interlayer with previously reported interlayer designs. Figure 2e shows that the large-sized pores ($>1\text{ }\mu\text{m}$) in the original SiNP-CNT layer shrank to nanopores after the first electrochemical lithiation. The nanopores with reduced diameter after lithiation ($<100\text{ nm}$ pores) can constrain Li_{BCC} to be deposited in small characteristic sizes inside the $\text{Li}_{3.75}\text{Si}$ -CNT layer, thereby making diffusion-enabled creep a dominant flow mechanism. In addition, this nanoporous Si can provide uniform lithophilic sites to depress nucleation barrier and suppress dendritic lithium formation.^[17]

Two levels of stack pressure of 5 and 65 MPa are applied to cells to evaluate the effect of stack pressure on cell performance. Figure 2g,e shows the size of the resultant pores (the interparticle gap between $\text{Li}_{3.75}\text{Si}$) under stack pressures of 5 and 65 MPa, respectively. The pore sizes were smaller when the applied external stack pressure was higher. For the observation of pores more clearly for the sample with stack pressure of 65 MPa, additional SEM images are shown in Figure S3 in the Supporting Information and a cross-sectional SEM image of $\text{Li}_{3.75}\text{Si}$ -CNT layer after ion beam milling process is shown in Figure S4 in the Supporting Information. Interestingly, the

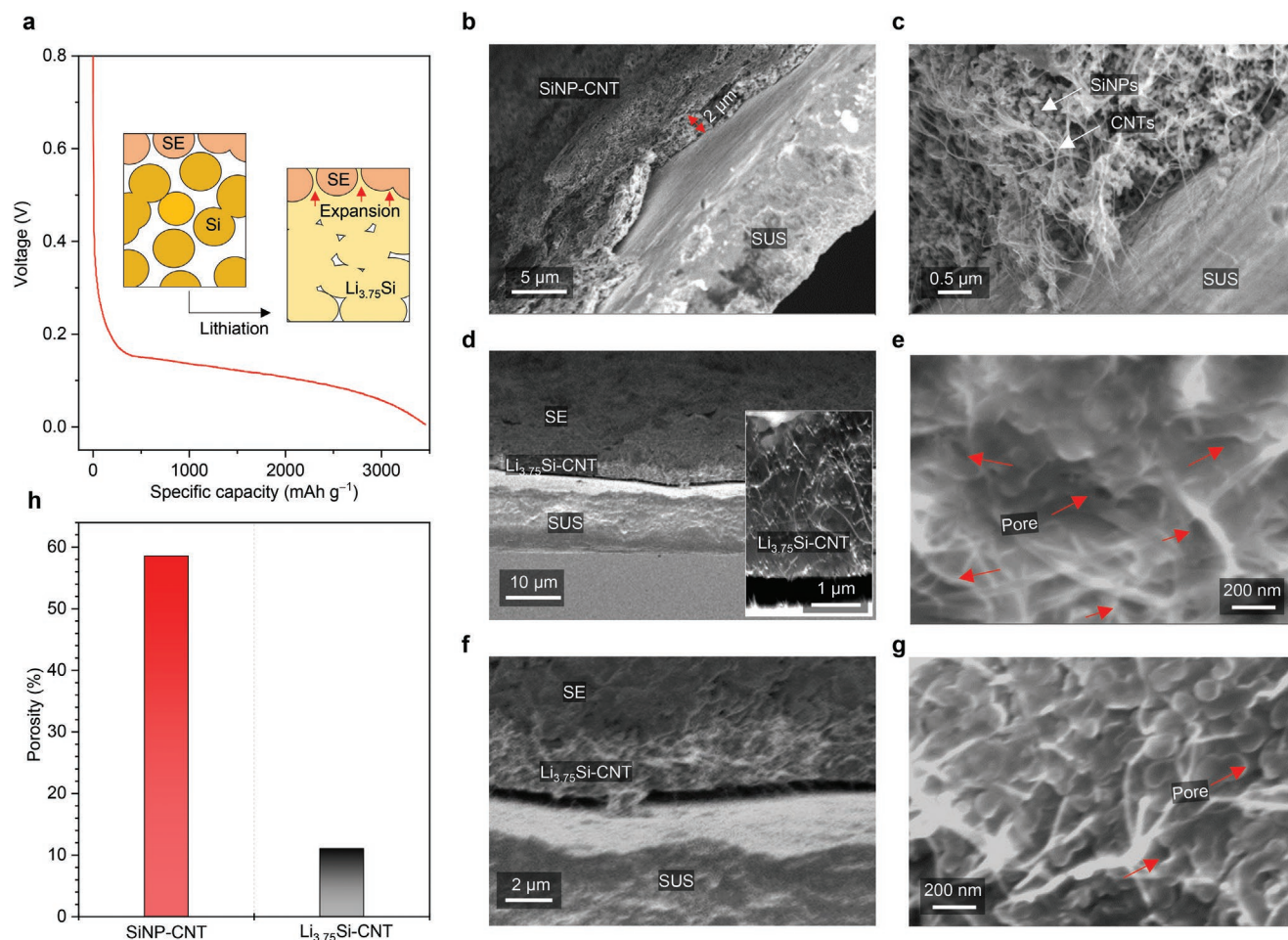


Figure 2. Electrochemical lithiation for fabrication of $\text{Li}_{3.75}\text{Si-CNT}$ interlayer. a) Voltage profile of SiNP-CNT electrode in ASSB (SUS/SiNP-CNT/SE/LiBCC) with an inset indicating the morphological change during lithiation. b, c) Cross-sectional SEM images of SiNP-CNT. d) Cross-sectional SEM image of $\text{Li}_{3.75}\text{Si-CNT}$ layer with an inset showing magnified image. This layer was obtained after the charging process of SiNP-CNT at a cut-off voltage of 5 mV under stack pressure of 65 MPa. e) Top-viewed SEM image of $\text{Li}_{3.75}\text{Si-CNT}$ layer (red arrows indicate the pores) under stack pressure of 65 MPa. f) Cross-sectional SEM image of $\text{Li}_{3.75}\text{Si-CNT}$ layer. g) Top-viewed SEM image of $\text{Li}_{3.75}\text{Si-CNT}$ layer produced under stack pressure of 5 MPa (red arrows indicate the pores). h) The porosity of SiNP-CNT (58.5%) and $\text{Li}_{3.75}\text{Si-CNT}$ layer (11.0%) is calculated based on the thickness and density of each layer.

$\text{Li}_{3.75}\text{Si-CNT}$ layer and the SE remained fully adherent after the disassembly of the cell for both stack pressures, while the interface between the $\text{Li}_{3.75}\text{Si-CNT}$ and the SUS CC showed a small gap (Figure 2f). Strong and spatially uniform adhesion of MIEC interlayer to SE is required to prevent localization of current densities. The formation of such a seamless interface has been assisted by the volumetric expansion caused by the lithiation of Si to $\text{Li}_{3.75}\text{Si}$ during charging, which introduces compressive stress to the SE, combined with the ductile (soft) properties of $\text{Li}_{3.75}\text{Si}$ and $\text{Li}_6\text{PS}_5\text{Cl}$.

To check compatibility between SiNP-CNT (or $\text{Li}_{3.75}\text{Si-CNT}$) with SE ($\text{Li}_6\text{PS}_5\text{Cl}$), XRD analyses of SUS/SE/ $\text{Li}_{3.75}\text{Si-CNT}$, SUS/SE/SiNP-CNT stacks, and SE were conducted as shown in Figure S5 in the Supporting Information. For all three XRD results, we observed no changes in $\text{Li}_6\text{PS}_5\text{Cl}$ crystalline structures regardless of the lithiation status of the SiNP-CNT layer. The stack with the SiNP-CNT layer showed XRD peaks indicating crystalline-Si. For the stack with the $\text{Li}_{3.75}\text{Si-CNT}$, those peaks no longer exist; instead,

the peaks indicating the crystalline- $\text{Li}_{3.75}\text{Si}$ appeared in XRD analysis as shown in Figure S6 in the Supporting Information—since the formation of $\text{Li}_{22}\text{Si}_5$ requires a much higher temperature, $\text{Li}_{3.75}\text{Si}$ is the fully lithiated state at the testing temperature.^[16,18] Despite no electrolytes in the SiNP-CNT layer, SiNPs can be fully lithiated because 1) volume expansion accompanied by Li-Si alloying reaction increases the true contact area between SiNPs, thus securing percolating pathways for charge carriers, 2) $\text{Li}_{3.75}\text{Si}$ itself has a higher ionic and electronic conductivities than pure Si, which makes it a “good” MIEC. During discharge of the SUS/SE/ $\text{Li}_{3.75}\text{Si-CNT}$, we also can see the voltage plateau indicating delithiation of crystalline- $\text{Li}_{3.75}\text{Si}$ (Figure S7, Supporting Information) which is commonly seen in LIBs.^[19] Based on these results, the interlayer thickness and material density of the $\text{Li}_{3.75}\text{Si}$ phase were obtained, and we calculated the porosity of the SiNP-CNT to be 58.5 vol% and the $\text{Li}_{3.75}\text{Si-CNT}$ layer to be 11.0 vol%, as shown in Figure 2h and Table S2 in the Supporting Information.

2.2. Behavior of Li_{Metal} Deposition/Stripping with $\text{Li}_{3.75}\text{Si-CNT}$ MIEC Interlayer

To check the impact of the $\text{Li}_{3.75}\text{Si-CNT}$ interlayer on the ASSB, electrochemical characterization of half-cells with and without the $\text{Li}_{3.75}\text{Si-CNT}$ interlayer was conducted. The configuration of the cells compared was as follows: $\text{SUS}/\text{Li}_{3.75}\text{Si-CNT}/\text{SE}/\text{Li}_{\text{BCC}}$ (same as the cell with $\text{SUS}/\text{SiNP-CNT}/\text{SE}/\text{Li}_{\text{BCC}}$ after lithiation of Si) and $\text{SUS}/\text{SE}/\text{Li}_{\text{BCC}}$, respectively, where SE is $\text{Li}_6\text{PS}_5\text{Cl}$. After electrochemical lithiation of SiNP-CNT to form $\text{Li}_{3.75}\text{Si-CNT}$ (cut-off discharge voltage: 5 mV), it was further discharged at a current density of -0.13 mA cm^{-2} for Li plating for 20 h (areal capacity: 2.55 mAh cm^{-2}) and charged at a current density of 0.25 mA cm^{-2} for Li stripping. The cut-off voltage of 200 mV was applied in Li stripping for $\text{Li}_{3.75}\text{Si-CNT}$ to avoid Li_xSi delithiation that potentially can cause severe morphological change due to the volume shrinkage.

At the beginning of Li deposition in the first cycle, there were significant voltage dip and flat voltage plateau (Figure 3a). The difference between the bottom of the voltage dip and the voltage plateau corresponds to Li_{BCC} nucleation overpotential. The nucleation overpotential of $\text{SUS}/\text{Li}_{3.75}\text{Si-CNT}/\text{SE}/\text{Li}_{\text{BCC}}$ and $\text{SUS}/\text{SE}/\text{Li}_{\text{BCC}}$ was 1.5 and 14.2 mV, respectively. Almost ten times lower nucleation overpotential in $\text{SUS}/\text{Li}_{3.75}\text{Si-CNT}/\text{SE}/\text{Li}_{\text{BCC}}$ is probably attributed to the high surface area of porous lithophilic $\text{Li}_{3.75}\text{Si-CNT}$ interlayer, which offers numerous sites for accomplishing the charge-transfer reaction $\text{Li}^*(\text{MIEC}) \leftrightarrow \text{Li}^+ + \text{e}^-$, as well as Li_{BCC} nucleation sites, effectively increasing the “true contact area” between SE and CC (see Figure 3a insets). On the other hand, in $\text{SUS}/\text{SE}/\text{Li}_{\text{BCC}}$ cell configuration, the charge-transfer reaction and nucleation sites are limited to physical contact points (area) at the interface between SUS and SE, and microscopically rough surfaces make the true contact area potentially much smaller than nominal contact area.^[20]

Notably, there were two voltage dips in $\text{SUS}/\text{Li}_{3.75}\text{Si-CNT}/\text{SE}/\text{Li}_{\text{BCC}}$ as shown in the inset of Figure 3a. Since there exist pores inside the $\text{Li}_{3.75}\text{Si-CNT}$ interlayer and Li_{BCC} gets deposited at the MIEC/CC interface, these could correspond to different physical processes, such as Li^* clustering on MIEC inner surface, Li_{BCC} nucleation on MIEC inner surface ($\text{Li}_{\text{BCC}}(\text{MIEC})$), Li_{BCC} nucleation closer to the CC ($\text{Li}_{\text{BCC}}(\text{MIEC}@CC)$), etc. If we hypothesize that the second voltage dip arises upon Li_{BCC} nucleation at the $\text{SUS}/\text{Li}_{3.75}\text{Si-CNT}$ interface, the $\text{Li}_{\text{BCC}}(\text{MIEC}@CC)$ is expected to be observed only after the later voltage dip. To explore the Li_{BCC} nucleation characteristics, we examined two sets of $\text{Li}_{3.75}\text{Si-CNT}$ interlayer, each of which was detached from SUS after Li plating up to 0.05 and 0.1 mAh cm^{-2} , respectively. Only the latter cell manifested the second voltage dip. SEM images in Figure S8 in the Supporting Information display the SUS-side surface of the former interlayer and exhibit a relatively smooth surface with a limited number of apparent pores, which implies that Li_{BCC} growth inside the $\text{Li}_{3.75}\text{Si-CNT}$ layer fills out the pores. In contrast, SEM images of the latter interlayer shown in Figure S9 in the Supporting Information exhibit some black plates covering $\text{Li}_{3.75}\text{Si-CNT}$, indicating that the Li_{BCC} deposition occurred between the $\text{Li}_{3.75}\text{Si-CNT}$ layer and SUS, while some pores of $\text{Li}_{3.75}\text{Si-CNT}$ layer may remain not completely filled. In line with this finding, XRD analysis (Figure 3b) shows that Li_2S derived from the

decomposition of $\text{Li}_6\text{PS}_5\text{Cl}$ is clearly present in the $\text{SUS}/\text{SE}/\text{Li}_{\text{BCC}}$ configuration after Li deposition ($-2.55 \text{ mAh cm}^{-2}$), while there are less Li_2S in $\text{SUS}/\text{Li}_{3.75}\text{Si-CNT}/\text{SE}/\text{Li}_{\text{BCC}}$. Less decomposition of SE in the interlayer-containing half-cell indicates that the supply of fresh neutral Li atoms to the $\text{Li}_{3.75}\text{Si-CNT}/\text{SE}$ interface is kinetically limited; an alternative explanation is that the porous $\text{Li}_{3.75}\text{Si-CNT}$ interlayer acts as a filter that forbids Li_2S or broken-off argyrodite particles to be transported into the suburbs, while still allowing Li^+/Li^* to pass in and out.

Given the post-mortem SEM images and XRD results, we believe that the newly formed Li^* accumulates mainly at the $\text{SUS}/\text{Li}_{3.75}\text{Si-CNT}$ interface rather than the $\text{Li}_{3.75}\text{Si-CNT}/\text{SE}$ interface. Preferential deposition at the $\text{SUS}/\text{Li}_{3.75}\text{Si-CNT}$ interface may have become possible by not only the enhanced adhesion of the interface between $\text{Li}_{3.75}\text{Si-CNT}$ and SE but also sufficient Li^* ad-atom diffusion rate through the $\text{Li}_{3.75}\text{Si-CNT}$ interlayer, like millions of commuters choosing to sleep every night in suburbs tens of miles away from their workplaces. Such stable and “off-city-center” Li_{BCC} deposition behavior in $\text{SUS}/\text{Li}_{3.75}\text{Si-CNT}/\text{SE}/\text{Li}_{\text{BCC}}$ brings about high reversibility of Li inventory “tidal waves” during the charging and discharging process. Accordingly, when the charge capacity portion coming from the lithiation of Si (0.68 mAh cm^{-2}) is subtracted, the $\text{SUS}/\text{Li}_{3.75}\text{Si-CNT}/\text{SE}/\text{Li}_{\text{BCC}}$ cell has an initial Coulombic efficiency of 96.4%, which is much higher than the 89.4% in $\text{SUS}/\text{SE}/\text{Li}_{\text{BCC}}$ configuration (Figure 3c).

To further prove the interpretation above, we investigated the Li_{BCC} morphology and location in each cell during the Li_{BCC} plating and stripping process. The cross-sectional SEM images and its corresponding energy-dispersive X-ray spectroscopy (EDS) for $\text{SUS}/\text{Li}_{3.75}\text{Si-CNT}/\text{SE}/\text{Li}_{\text{BCC}}$ show uniform and dense deposition of Li_{BCC} between $\text{Li}_{3.75}\text{Si-CNT}$ and SUS CC after plating (Figure 3d,f), while the $\text{Li}_{3.75}\text{Si-CNT}$ interlayer preserves its original shape without significant morphological changes (Figure 3e). After subsequent Li stripping, the Li_{BCC} completely disappears and the SUS CC exhibits a clean surface (Figure 3g,h). On the other hand, $\text{SUS}/\text{SE}/\text{Li}_{\text{BCC}}$ shows that the deposited Li_{BCC} has a porous structure, and some of the powders suspected as SE are embedded in the Li_{BCC} layer (Figure 3i,k). Moreover, there are regions with partially deposited Li_{Metal} , indicating that inhomogeneous Li_{Metal} deposition occurs in $\text{SUS}/\text{SE}/\text{Li}_{\text{BCC}}$ half-cell. Such inhomogeneous deposition is more severe after Li stripping, where Li_{Metal} with random shape still exists on the CC in both cross-sectional SEM images and the photograph shown in Figure 3l,m. Such random deposition can increase localized current density and consequently vary the local pressure, which encourages Li_{Metal} dendrite growth at the interface with SE in ASSB during further cycling of the cell (Figure 3j).

2.3. Identifying Functions of Each Component in $\text{Li}_{3.75}\text{Si-CNT}$ MIEC Interlayer

To further understand the role of the silicide and CNTs in the $\text{Li}_{3.75}\text{Si-CNT}$ layer, we compared the $\text{SUS}/\text{Li}_{3.75}\text{Si-CNT}/\text{SE}/\text{Li}_{\text{BCC}}$ and other asymmetric cell configurations, including only the CNTs (denoted as $\text{SUS}/\text{CNT}/\text{SE}/\text{Li}_{\text{BCC}}$) and $\text{Li}_{3.75}\text{Si}$ layer without CNTs (denoted as $\text{SUS}/\text{Li}_{3.75}\text{Si}/\text{SE}/\text{Li}_{\text{BCC}}$). The

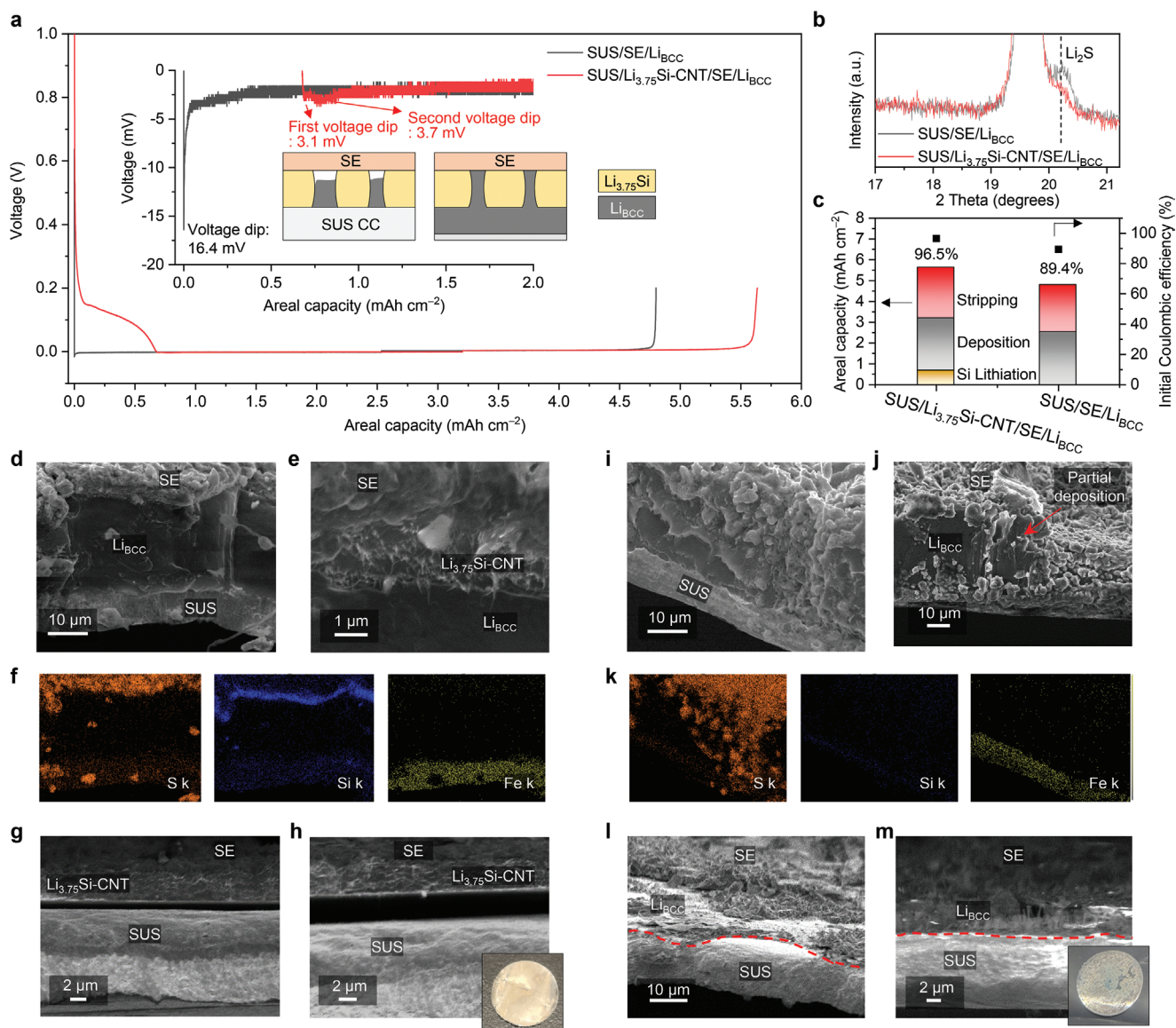


Figure 3. Investigation of interface depending on the existence of $\text{Li}_{3.75}\text{Si-CNT}$. a) Voltage profiles of half-cells ($\text{SUS}/\text{Li}_{3.75}\text{Si-CNT}/\text{SE}/\text{Li}_{\text{BCC}}$ and $\text{SUS}/\text{SE}/\text{Li}_{\text{BCC}}$) at the first cycle. The inset shows a magnified voltage profile indicating the overpotential of each cell and a schematic illustration of the Li metal deposition process in the $\text{Li}_{3.75}\text{Si-CNT}$ layer located between SE and the CC. 3.1 and 16.4 mV indicate the first voltage dip of $\text{SUS}/\text{Li}_{3.75}\text{Si-CNT}/\text{SE}/\text{Li}_{\text{BCC}}$ and $\text{SUS}/\text{SE}/\text{Li}_{\text{BCC}}$, respectively. b) XRD analysis (Mo $K\alpha$ of wavelength 0.7107 Å) of SE surface contacting with $\text{Li}_{3.75}\text{Si-CNT}$ and SUS in $\text{SUS}/\text{Li}_{3.75}\text{Si-CNT}/\text{SE}/\text{Li}_{\text{BCC}}$ and $\text{SUS}/\text{SE}/\text{Li}_{\text{BCC}}$, respectively, after Li deposition process. c) Bar graphs showing the areal capacity and the initial Coulombic efficiency of the half-cells with or without the $\text{Li}_{3.75}\text{Si-CNT}$. Different color is used to distinguish the areal capacity corresponding to different physical processes: Si lithiation (yellow), Li deposition (gray), and stripping (red). d–h) Cross-sectional SEM images of d,e) $\text{SUS}/\text{Li}_{3.75}\text{Si-CNT}/\text{SE}/\text{Li}_{\text{BCC}}$ after Li deposition and f) its corresponding EDS mapping as well as g,h) after Li stripping with an inset of the photograph of SUS CC detached from SE. i–m) Cross-sectional SEM images of i,j) $\text{SUS}/\text{SE}/\text{Li}_{\text{BCC}}$ after Li deposition and k) its corresponding EDS mapping as well as l,m) after Li stripping with an inset of the photograph of SUS CC detached from SE. Areal capacity of 3 mAh cm^{-2} was applied for the Li deposition and stripping as described in the Experimental Section.

$\text{SUS}/\text{CNT}/\text{SE}/\text{Li}_{\text{BCC}}$ cell showed a lower Li_{BCC} nucleation overpotential than that of $\text{SUS}/\text{SE}/\text{Li}_{\text{BCC}}$, likely due to the high surface area of CNTs with many contact points with SE which offers numerous nucleation sites in the first cycle (Figure 4a). However, CNTs with relatively low ionic conductivity (compared to SE) likely cause excessive Li_{BCC} plating at the CNT/SE interface, where Li_{BCC} can directly contact and react with SE, causing severe decomposition similar to the $\text{SUS}/\text{SE}/\text{Li}_{\text{BCC}}$

cell. This is similar to the salaryman (Li^+) easily finding his car (e^-) near the city center, but there is no good highway to the suburbs, causing traffic jams near the city center. The decomposition reactions concentrated at the interface can induce continued stress concentration and the formation of large cracks in SE, eventually leading to cell short-circuiting.^[6] On the other hand, we observed that $\text{SUS}/\text{Li}_{3.75}\text{Si}/\text{SE}/\text{Li}_{\text{BCC}}$ exhibits outstanding stability and cyclability without any short-circuiting for

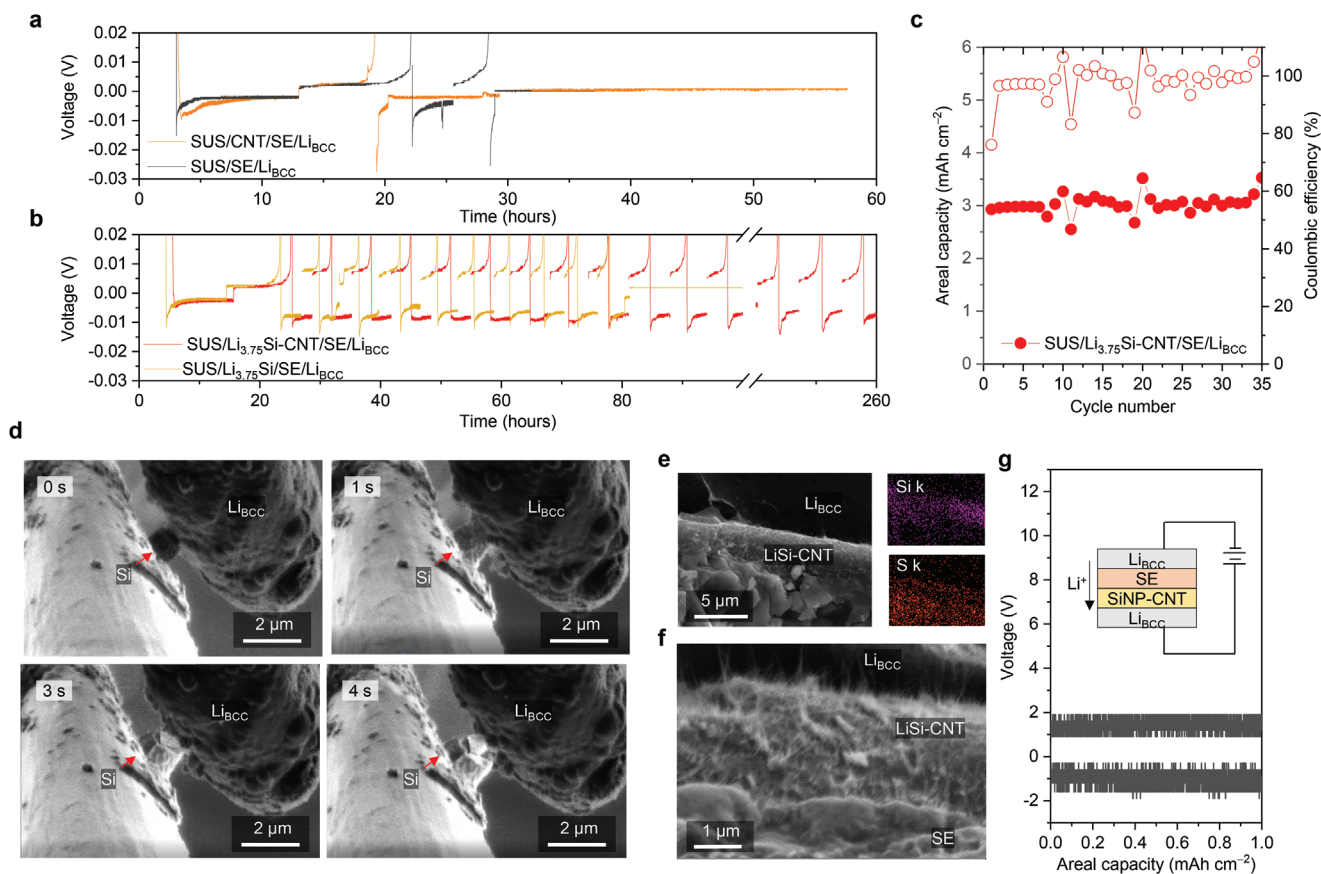


Figure 4. Electrochemical characterization of various interlayers. a) The cyclic performance of SUS/CNT/SE/Li_{BCC} and SUS/SE/Li_{BCC} (half-cell, asymmetric cells) at a current density of 0.1 and 0.3 mA cm⁻² for the first (10 h) and the rest of the cycles (3.3 h), respectively (areal capacity: 1.0 mAh cm⁻²). b) The cyclic performance of SUS/Li_{3.75}Si-CNT/SE/Li_{BCC} and SUS/Li_{3.75}Si/SE/Li_{BCC} at a current density of 0.3 and 0.92 mA cm⁻² of the first (10 h) and the rest of the cycles (3.3 h), respectively (areal capacity: 3.0 mAh cm⁻²). c) Areal capacity retention and Coulombic efficiency of SUS/Li_{3.75}Si-CNT/SE/Li_{BCC} in a half-cell. d) Observations of silicon particle contacting Li_{BCC} (nonelectrochemical lithiation) through the in situ SEM. e) Cross-sectional SEM image and its corresponding EDS mapping images of nonelectrochemically lithiated SiNP-CNT interlayer—nonelectrochemical lithiation refers to lithiation driven by physical contact between SiNP-CNT and Li_{BCC} foil—in the cell of Li_{BCC}/SiNP-CNT/SE/NCM811. f) Magnified cross-sectional SEM images of LiSi-CNT interlayer in Li_{BCC}/SiNP-CNT/SE/NCM811. g) Voltage profile of symmetric cell (Li_{BCC}/SE/Si/Li_{BCC}) with an inset showing its circuit diagram.

80 h even at a higher current density of 0.30 and 0.92 mA cm⁻² (Figure 4b) in contrast to SUS/CNT/SE/Li_{BCC} and SUS/SE/Li_{BCC}. One of the reasons for the relatively high stability of the SUS/Li_{3.75}Si/SE/Li_{BCC} cell is the electrochemical stability of the Li_{3.75}Si against the SE layer, as discussed earlier. Also, interweaving CNTs with the Li_{3.75}Si particles was seen to greatly improve the cycle life (>250 h), and it also provides high Coulombic efficiency (99.3%, average value for 35 cycles) and no capacity degradation, as shown in Figure 4c (see cycle life and corresponding Coulombic efficiency of SUS/Li_{3.75}Si/SE/Li in Figure S10, Supporting Information). Both Si and carbon are earth-abundant elements that are commercially available at low cost, and the aforementioned results highlight the synergistic roles of CNT and silicides in improving the ASSB performance.

Generally, interparticle contact between SiNPs as well as their adhesion to the SUS CC is poor without a binder; thus, SiNP compact often experiences particle contact loss and SiNP/SUS interface decohesion. Such phenomena could hinder the interlayer from functioning even after the lithiation of the SiNPs. For ASSBs, even though polymer-based binders can be used to glue the Li_{3.75}Si particles together to form a tougher compact,

they could increase the interfacial resistance owing to their low electrical and ionic conductivities. Herein the wrapping-around CNTs act as a binder during the electrode fabrication process of SiNP-CNT because their outstanding mechanical characteristics (high modulus of about 1 TPa and high tensile strength of more than 10 GPa) improve the integrity of the networking structure of the interlayer during fabrication as well as electrochemical cycling process.^[21] In other words, CNT-added SiNPs work like reinforced concrete, in which the relatively low strength and ductility of pure concrete, especially in tension, are enhanced by steel bars having higher tensile strength and ductility. Such mechanically reinforced Li_{3.75}Si-CNT interlayer preserving morphological integrity further strengthens its function as a strain buffer. As proof of this assertion, under the harsh mechanical environment of bent Li_{3.75}Si-CNT interlayers (see Figure S11 in the Supporting Information. The interlayer was repeatedly bent by about 40°–50° ten times), the fact that CNTs seem to be pulled taut to prevent the fracture of Li_{3.75}Si was discovered in the SEM top-viewed images. Moreover, the homogenous distribution of 1D CNTs with high electronic conductivity not only helped the formation of uniform Li_{3.75}Si during electrochemical

lithiation but also induced better plating and stripping of Li_{BCC} phases inside and in contact with $\text{Li}_{3.75}\text{Si}$ -CNT compared to the cell without CNTs ($\text{SUS}/\text{Li}_{3.75}\text{Si}/\text{SE}/\text{Li}_{\text{BCC}}$). For these reasons, we believe that $\text{SUS}/\text{Li}_{3.75}\text{Si}$ -CNT/SE/ Li_{BCC} cell showed the longest cycle life without short-circuiting.

2.4. Full-Cell Evaluations

To check the practical feasibility of the $\text{Li}_{3.75}\text{Si}$ -CNT interlayer, a full ASSB cell containing a cathode needs to be evaluated. Moreover, electrochemical lithiation of SiNPs before operating a cell is required for the formation of our $\text{Li}_{3.75}\text{Si}$ -CNT interlayer, which means that an additional Li source is required. Therefore, it is necessary for the full-cell to include an additional amount of cyclable Li; such an additional Li inventory can come from the cathode. However, an extra amount of cathode material that is used only for the formation of $\text{Li}_{3.75}\text{Si}$ -CNT will decrease the full-cell energy density and increase resistance in the aspect of cell design (e.g., the high areal capacity of the electrode could result in high cell resistance) due to thicker cathode electrode. Since we have noticed that the Si functions as a lithophilic material which promotes good wetting with molten Li ,^[22] nonelectrochemical lithiation or mechanical lithiation was considered. Briefly, Si physically contacting Li_{BCC} could be lithiated and transformed to lithium silicide in the absence of electrochemical current to avoid the extra cathode loading in a full-cell. To confirm that solid-state Li_{Metal} also can give rise to smooth lithiation of the microns-thick SiNP-CNT layer, in situ SEM analysis was conducted using a single micron-sized Si particle (Figure 4d). We monitored that the Si particle was lithiated for a few seconds and expanded, which is commonly observed in the LIB Si anode material.^[16] Based on this experimental observation, we adopted an approach to fabricate a full-cell by inserting thin Li_{BCC} foil ($\approx 30\ \mu\text{m}$ thick as shown in Figure S12, Supporting Information) between the CC and SiNP-CNT layer. The full-cell with NCM811 cathode (denoted as $\text{Li}_{\text{BCC}}/\text{SiNP-CNT}/\text{SE}/\text{NCM811}$) was investigated and the cross-sectional SEM images and its corresponding EDS (Figure 4e) of the full-cell before cycling (i.e., without any electrochemical current) confirmed that SiNP-CNT layer was transformed to lithium silicide interlayer upon the cell assembly where the uniaxial pressure was applied. The magnified image in Figure 4f shows a highly densified lithium silicide-CNT layer similar to the one obtained by electrochemical lithiation of the half-cell of $\text{SUS}/\text{Li}_{3.75}\text{Si}/\text{SE}/\text{Li}_{\text{BCC}}$ (Figure 2d–g). In addition, the voltage plateau assigned to the alloying reaction of Si with Li is not seen in the voltage profile of a symmetric cell ($\text{Li}_{\text{BCC}}/\text{SiNP-CNT}/\text{SE}/\text{Li}_{\text{BCC}}$), as shown in Figure 4g, which also indicates that SiNP-CNT can be lithiated without external current by contacting thin Li_{BCC} foil.

Electrochemical characterization of the prepared full-cell ($\text{Li}_{\text{BCC}}/\text{SiNP-CNT}/\text{SE}/\text{NCM811}$) was conducted, and a full-cell of $\text{Li}_{\text{BCC}}/\text{SE}/\text{NCM811}$ was also fabricated for comparison. The cells were cycled between 2.8 and 4.3 V at 0.1 C for the first cycle and 0.35 C for the rest of the cycles (see the Experimental Section for the details of cell preparation and electrochemical measurements). The voltage profiles show that the initial specific capacity of cathode materials was similar in

each cell (2078 mAh g^{-1} for $\text{Li}_{\text{BCC}}/\text{SiNP-CNT}/\text{SE}/\text{NCM811}$ and 205.1 mAh g^{-1} for $\text{Li}_{\text{BCC}}/\text{SE}/\text{NCM811}$) (Figure 5a). The initial Coulombic efficiency of $\text{Li}_{\text{BCC}}/\text{SiNP-CNT}/\text{SE}/\text{NCM811}$ was 92.0%, being higher than that of $\text{Li}_{\text{BCC}}/\text{SE}/\text{NCM811}$ (86.5%) (Figure 5b). This result indicates that $\text{Li}_{3.75}\text{Si}$ -CNT pre-formed by reacting SiNP-CNT with the Li_{BCC} foil prevented direct contact between Li_{BCC} and SE and chemical reduction of $\text{Li}_6\text{PS}_5\text{Cl}$ SE, which matches with the results of the half-cell. More interestingly, the de-alloying reaction of $\text{Li}_{3.75}\text{Si}$ (assigned to a range of 3.2–3.4 V in the full-cell) does not show up in the voltage profile during discharging to a cut-off voltage of 2.8 V. This is because Li_{BCC} foil used for lithiation of SiNP-CNT supplies enough source of Li to the cathode, and the delithiation potential of $\text{Li}_{3.75}\text{Si}$ is higher than the stripping potential of Li_{Metal} (i.e., the electrochemical de-alloying reaction of $\text{Li}_{3.75}\text{Si}$ would start if there is no other lithium source in anode). Therefore, the $\text{Li}_{3.75}\text{Si}$ -CNT MIEC layer here functions not as an anode-active material, but as a ground for charge-transfer reaction $\text{Li}^* \leftrightarrow \text{Li}^+ + \text{e}^-$ (“parking lot”), a highway for transportation of Li^* ad-atoms and e^- , and nucleation site and creep channel of Li_{BCC} phases. In contrast, delithiation of $\text{Li}_{3.75}\text{Si}$ occurred during discharging in $\text{SiNP-CNT}/\text{SE}/\text{NCM811}$ without excess Li inventory, as can be seen from the voltage profile displayed in Figure S13 in the Supporting Information.

Full-cell cycling performance of $30\ \mu\text{m-Li}_{\text{BCC}}/\text{SiNP-CNT}/\text{SE}/\text{NCM811}$ shows capacity retention of 94.6% after 100 cycles and 88.9% after 200 cycles, while the Coulombic efficiency reaches 99.9% after tens of cycles. On the other hand, drastic capacity fading was observed for the full-cell without the $\text{Li}_{3.75}\text{Si}$ -CNT interlayer ($30\ \mu\text{m-Li}_{\text{BCC}}/\text{SE}/\text{NCM811}$) just after 30 cycles. The stack pressure was found to highly affect cell degradation for the $30\ \mu\text{m-Li}_{\text{BCC}}/\text{SE}/\text{NCM811}$. The cell under a high stack pressure of 65 MPa showed a sudden capacity drop due to short-circuiting (see Figure S14a, Supporting Information) as compared to low stack pressure of 34 MPa. However, the cell containing the $\text{Li}_{3.75}\text{Si}$ -CNT interlayer shows outstanding electrochemical performance regardless of stack pressure (voltage profiles of $30\ \mu\text{m-Li}_{\text{BCC}}/\text{SiNP-CNT}/\text{SE}/\text{NCM811}$ at stack pressure of 5 MPa are shown in Figures S14b,c, Supporting Information). These results indicate that the $\text{Li}_{3.75}\text{Si}$ -CNT interlayer enables the ASSB systems to operate at lower stack pressures. To investigate the effect of the pore size inside the $\text{Li}_{3.75}\text{Si}$ -CNT interlayer on the cycling performance of the full-cells, we applied different stack pressures of 5 MPa as from the fabrication process of ASSB. Then the stack pressure of 65 MPa was applied after first cycle. This is because 5 MPa stack pressure during the formation of $\text{Li}_{3.75}\text{Si}$ -CNT interlayer (lithiation of SiNPs) leads to relatively large-sized pores than those formed under 65 MPa as discussed before (see Figure 2j). The cell ($\text{Li}_{\text{BCC}}/\text{SiNP-CNT}/\text{SE}/\text{NCM811}$) under such evaluation condition shows short-circuiting after 21 cycles, as shown in Figure S15 in the Supporting Information. These results indicate that relatively large-sized Li_{BCC} formed inside large pores has higher hardness than nanosized Li_{BCC} (according to the “larger is much harder” trend as illustrated in Figure 1a), and therefore such $\text{Li}_{\text{BCC}}@$ MIEC can induce mechanical displacement and penetration of SE during lithium deposition.

The rate capability of the full-cell with $\text{Li}_{3.75}\text{Si}$ -CNT interlayer ($30\ \mu\text{m-Li}_{\text{BCC}}/\text{SiNP-CNT}/\text{SE}/\text{NCM811}$) was studied by varying

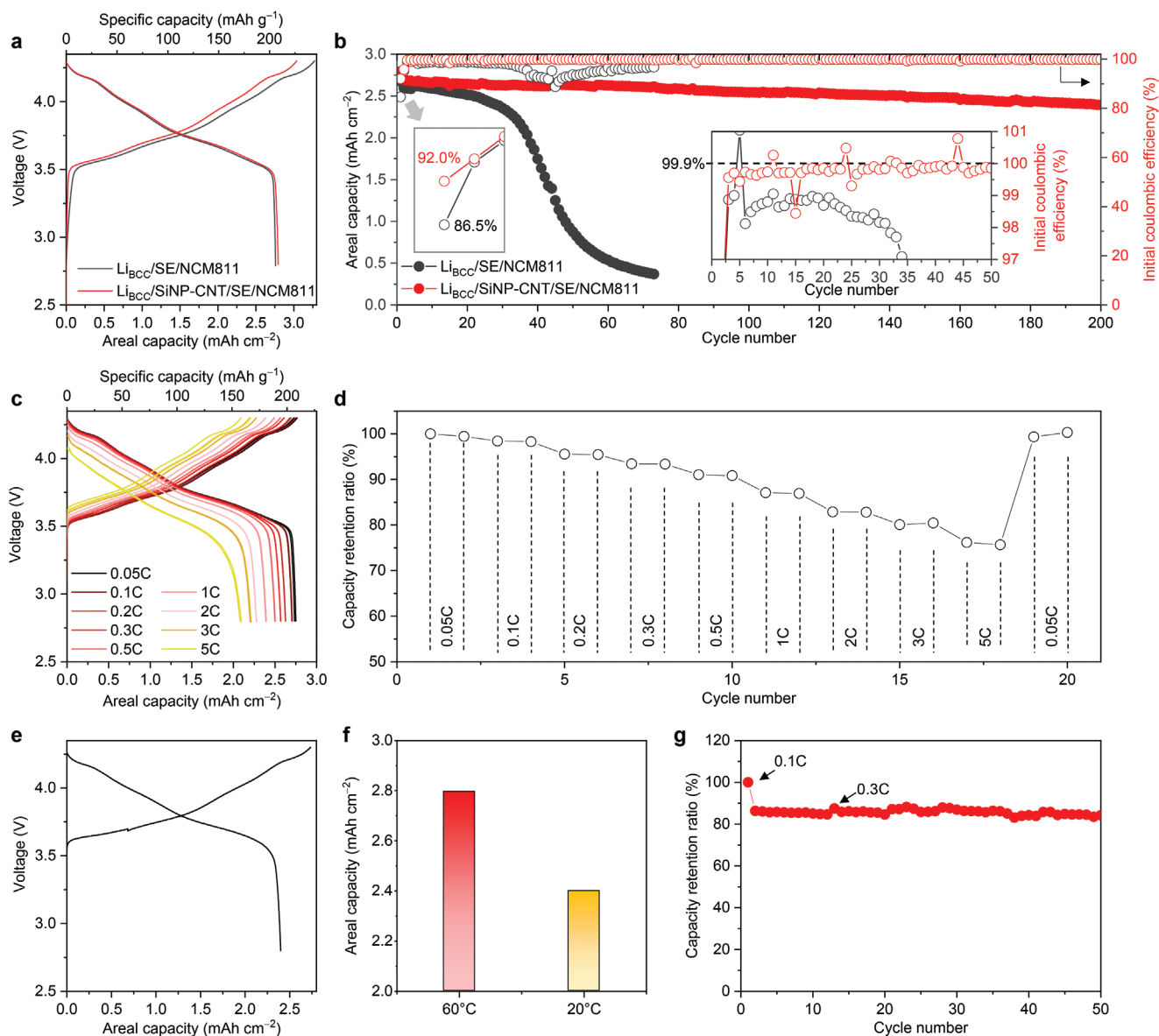


Figure 5. Electrochemical characterization (full-cell) with $\text{Li}_{3.75}\text{Si-CNT}$ MIEC interlayer. a) Charge and discharge profile of $\text{Li}_{\text{BCC}}/\text{SE}/\text{NCM811}$ and $\text{Li}_{\text{BCC}}/\text{SiNP-CNT}/\text{SE}/\text{NCM811}$ for the first cycle under stack pressure of 34 and 65 MPa, respectively. b) Areal capacity retention and Coulombic efficiency of $\text{Li}_{\text{BCC}}/\text{SE}/\text{NCM811}$ and $\text{Li}_{\text{BCC}}/\text{SiNP-CNT}/\text{SE}/\text{NCM811}$ at an operating temperature of 60 °C. Insets exhibit the magnified graph of (initial) Coulombic efficiency for the first cycle and 50th cycles. c) Voltage profile and d) capacity retention ratio of $\text{Li}_{\text{BCC}}/\text{SiNP-CNT}/\text{SE}/\text{NCM811}$ at different C-rates. e) Voltage profiles of $\text{Li}_{\text{BCC}}/\text{SiNP-CNT}/\text{SE}/\text{NCM811}$ at 20 °C. f) Comparison of the areal capacity of $\text{Li}_{\text{BCC}}/\text{SiNP-CNT}/\text{SE}/\text{NCM811}$ at different operating temperatures. g) Capacity retention ratio of $\text{Li}_{\text{BCC}}/\text{SiNP-CNT}/\text{SE}/\text{NCM811}$ at 20 °C.

the discharge rate from 0.05 C to 5 C at a fixed charge rate of 0.05 C in a constant current mode, and we observed that the discharge capacity was about 82.8% at 2 C and 76% at 5 C as compared to the original capacity at 0.05 C (Figure 5c,d). Furthermore, the discharge capacity and cyclability at low temperatures were investigated, which is a critical decision point for battery application in the electric vehicles industry. As the temperature decreased to 20 °C, the areal capacity of the 30 $\mu\text{m-Li}_{\text{BCC}}/\text{SiNP-CNT}/\text{SE}/\text{NCM811}$ was 2.4 mAh cm^{-2} , which is 85.8% of the areal capacity obtained at 60 °C (Figure 5e). The capacity was sustained without a significant decrease and remained at 97.65% after 49 cycles (Figure 5f).

Post-mortem analysis using each full-cell (after 200 cycles for 30 $\mu\text{m-Li}_{\text{BCC}}/\text{SiNP-CNT}/\text{SE}/\text{NCM811}$ and 73 cycles for 30 $\mu\text{m-Li}_{\text{BCC}}/\text{SE}/\text{NCM811}$, respectively) in the discharged state was conducted to examine the morphological change of Li_{BCC} , $\text{Li}_{3.75}\text{Si-CNT}$ layer, and their interfaces. As clearly shown in Figure 6a,b, the $\text{Li}_{3.75}\text{Si-CNT}$ layer not only separates the SE and Li_{BCC} but also preserves its morphological integrity without any spallation or deformation for the $\text{Li}_{\text{BCC}}/\text{SiNP-CNT}/\text{SE}/\text{NCM811}$ cell.

According to previous works on the inelastic deformation behavior of metals, interfacial diffusion-mediated Coble creep, which is one of the deformation mechanisms dominant at very

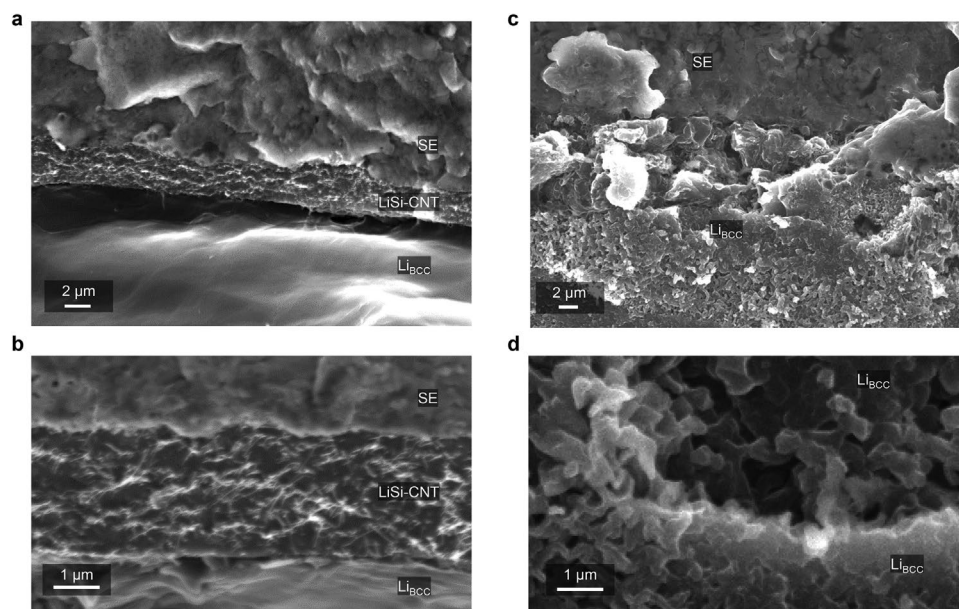


Figure 6. Post-mortem analysis of LiSi-CNT interlayer. a,b) Cross-sectional SEM images of Li_{BCC}/SiNP-CNT/SE/NCM811 after 200 cycles. c,d) Cross-sectional SEM images of Li_{BCC}/SE/NCM811 after 73 cycles.

small sample sizes,^[15c] can cause drastic softening of Li_{BCC}. The fracture of Li_{3,75}Si-CNT can be avoided by such small-sized Li_{BCC} formation within tiny pores during the Li plating process, which ensures the mechanical stability of both Li_{3,75}Si-CNT and the soft SE. Furthermore, in order to cause a morphological change of Li_{3,75}Si (Young's modulus: 41 GPa and hardness: 1.9 GPa, absolute value), Li_{BCC} nucleated in the Li_{3,75}Si layer needs to afford the stress.^[23] However, the hardness and strength of the Li_{3,75}Si layer are much higher than the hardness ($\approx 7\text{--}43$ MPa) and strength of Li_{BCC}.^[8] Therefore, the creep of Li_{BCC} located inside the Li_{3,75}Si porous layer is inevitable. In addition, the tensile strength of Li_{3,75}Si-CNT enhanced by adding CNTs as well as the significantly reduced hardness of Li_{BCC} derived from its size effect (Figure 1a) further help to avoid the deformation and damage of the Li_{3,75}Si-CNT interlayer.

Densified Li_{BCC} deposit with a smooth surface exists even after 200 cycles because of the outstanding mechanical and transport properties of the Li_{3,75}Si-CNT interlayer (Figure S16a, Supporting Information), which coincides with the reversible Li plating/stripping phenomena described in Figure 3. In the case of the Li_{BCC}/SE/NCM811, there is a porous structure at the boundary between the SE and Li_{BCC} that likely is a side reaction product, and Li_{BCC} also has the feature of a porous and moss-like structure that might come from the inhomogeneous Li_{BCC} extrusion into SE and also inhomogeneous stripping upon repeated cycling (Figure 6c,d; the magnified cross-sectional SEM images of the Li_{BCC} side are shown in Figure S16b, Supporting Information).

3. Conclusion

In summary, we showed the significant role of an ultra-thin open 3D nanoporous Li_{3,75}Si-CNT MIEC interlayer (3.25 μm) in the electrochemical performance of an ASSB with argyro-

dite (Li₆PS₅Cl) SE. In the asymmetric cell of SUS/Li_{3,75}Si-CNT/SE/Li_{BCC} (achieved by electrochemical lithiation of SUS/SiNP-CNT/SE/Li_{BCC}), we observed that dense metallic Li forms and grows out between the CC and the Li_{3,75}Si-CNT interlayer, thereby the direct contact of Li_{BCC} to SE and decomposition of SE being limited. Such deposition behavior is attributed to the interlayer's 1) mixed conducting properties, maintaining long-range ionic/electronic percolations, 2) 3D nanoporosity, which offers numerous active sites for charge-transfer reaction ($\text{Li}^*/\text{MIEC} \leftrightarrow \text{Li}^+ + \text{e}^-$), and 3) high lithiophilicity, which reduces nucleation barrier and enables facile surface diffusion through the porous MIEC. In particular, small-sized pores constraining the deposited Li_{BCC} to be $\ll 100$ nm (smaller is much softer) mitigate the formation of Li_{Metal}-induced mechanical instabilities in the soft SE and the MIEC interlayer, while facilitating diffusional Li_{Metal} flow toward the reserved porosity. On the contrary, the cell without our MIEC interlayer experiences inhomogeneous Li_{Metal} deposition and massive formation of unwanted residues such as Li₂S during plating/stripping, which leads to poor Coulombic efficiency. The Li_{3,75}Si-CNT interlayer may also act as a filter of such broken-off argyrodite or Li₂S residues, while still allowing Li⁺/Li* to pass in and out. A full-cell made of 30 μm thick Li_{BCC} foil as Li inventory in contact with the MIEC interlayer (30 μm -Li_{BCC}/SiNP-CNT/SE/NCM811) demonstrated stable cycling stability of 88.9% after 200 cycles and 97.65% after 49 cycles at 60 and 20 $^\circ\text{C}$, respectively. On the other hand, drastic capacity fading was seen in the cell with the same configuration but without the MIEC interlayer (30 μm -Li_{BCC}/SE/NCM811). The nano-architected ultra-thin Li_{3,75}Si-CNT MIEC interlayer designed and tested in this work showed significant improvement in our ASSB cell. We believe that the results of this work may pave a path for achieving commercially feasible ASSB with high-energy density and improved safety using earth-abundant elements.

4. Experimental Section

Electrode Preparation: The SiNP-CNT electrode was fabricated using commercial SiNPs (Alfa Aesar), CNTs, and deionized water solvent (the mass ratio of SiNPs:CNTs was 90:10). The dispersion solution was mixed and stirred vigorously in a planetary centrifugal mixer (Thinky Corporation, AR-100), and it was cast on the stainless steel foil (thickness was ≈ 0.01 mm) up to ≈ 0.21 mg cm⁻². The electrode was then dried at 110 °C for 6 h in the vacuum oven. The other electrodes (SiNP and CNT) were fabricated under the same conditions described above.

Cell Preparation: All ASSBs in this study were fabricated using pellet cells (Canrd, China). For the half-cell, 90 mg powder-typed Li₆PS₅Cl (NEI Corporation, United States) was loaded in a pellet cell (diameter of 1 cm) and then pressed at 200 MPa. The prepared SiNP-CNT electrode and Li₆PS₅Cl separator layer were stacked together, and they were pressed together at 700 MPa. After that, the Li foil with a thickness of 0.350 mm (XIAMEN TOB new energy technology Co., LTD.) was put on the other side of SiNP-CNT electrode (denoted as SUS/SiNP-CNT/SE/Li_{BCC}). The half-cells which contained SUS CC and the electrode consisting of CNT on SUS CC were denoted as SUS/SE/Li_{BCC} and SUS/CNT/SE/Li_{BCC}, respectively. When the Si in the half-cells (SUS/SiNP/SE/Li_{BCC} and SUS/SiNP-CNT/SE/Li_{BCC}) was electrochemically lithiated, the cells were denoted as SUS/Li_{3.75}Si/SE/Li_{BCC} and SUS/Li_{3.75}Si-CNT/SE/Li_{BCC}, respectively. For the full-cell, niobium-coated NCM811, Li₆PS₅Cl, and carbon black (Super P, TIMCAL) were first mixed in a mortar at the weight ratio of 67:30:3, respectively. The prepared cathode mixture (20 mg cm⁻²), Li₆PS₅Cl, and SiNP-CNT electrodes were stacked together in this order and pressed at 700 MPa. Then, the Li_{BCC} foil (with a thickness of 30 μm) was inserted between the SUS CC and SiNP-CNT layer. As sulfide-based materials and Li were sensitive to air and moisture, all these procedures were done in an argon-filled glovebox (H₂O < 1.0 ppm, O₂ < 1.0 ppm).

Electrochemical Characterization: For electrochemical lithiation of SiNP-CNT electrode, a constant current of -0.3 mA cm⁻² (0.45 C) was applied until the cut-off voltage of 0.005 V. The electrochemical assessment (Li plating/stripping process) was carried out in the half-cell. For the SUS/SE/Li_{BCC} and SUS/CNT/SE/Li_{BCC}, a constant current of -0.1 mA cm⁻² was applied for 10 h for discharging and then it was charged at a constant current of 0.1 mA cm⁻² until the cut-off voltage of 0.2 V for the first cycle. Then a constant current of -0.3 mA cm⁻² was applied for 3.3 h for discharging and it was charged at a current of 0.3 mA cm⁻² until the cut-off voltage of 0.2 V for the rest of the cycles. The areal capacity was about 1.0 mAh cm⁻². For the SUS/Li_{3.75}Si/SE/Li_{BCC} and SUS/Li_{3.75}Si-CNT/SE/Li_{BCC}, a constant current of -0.3 mA cm⁻² was applied for 10 h for discharging, and it was charged a current of 0.3 mA cm⁻² until the cut-off voltage of 0.2 V at the first cycle. The constant current of -0.92 mA cm⁻² was applied for 3.3 h for discharging, and it was charged at a current of 0.92 mA cm⁻² until the cut-off voltage of 0.2 V for the rest of the cycles. The areal capacity was about 3.0 mAh cm⁻². The electrochemical assessment was conducted in the full-cell in a voltage range from 2.8 to 4.3 V at a rate of 0.1 C (constant current of 0.28 mA cm⁻²) for the first cycle and 0.35 C (constant current of 0.98 mA cm⁻²) for the rest of the cycles. Electrochemical analysis of all half-cells and full-cells was conducted using a battery cycler (Neware).

Material Characterization: Morphological investigation for the materials, electrode, and cells was conducted using SEM and EDS (Zeiss Merlin) and high-resolution TEM (JEM-2100F, JEOL). Sample preparation for cross-sectional view (Figure S4, Supporting Information) was carried out using ion milling system (IB-09020CP, JEOL). The two X-ray diffractometers (AERIS, Malvern PANalytical with Cu K α of wavelength 1.542 Å and Empyrean, Malvern PANalytical Mo K α of wavelength 0.7107 Å) were used for the physicochemical characterizations. The cells (SUS/SE/Li_{3.75}Si-CNT and SUS/SE/SiNP-CNT) were disassembled in an argon-filled glove box (H₂O < 1 ppm, O₂ < 1 ppm) and sealed by polyimide film to prevent its exposure to air, and the top side of the Li_{3.75}Si-CNT and SiNP-CNT was detected. To examine the morphological changes of the samples after cycling, the cycled cells were disassembled in an Ar-filled glove box (H₂O < 1 ppm, O₂ < 1 ppm) and then the

electrode was cut by scissors for cross-sectional SEM. For observation of micron-sized silicon lithiation (i.e., nonelectrochemical lithiation as mentioned in the Results and Discussion), in situ technique was conducted using SEM (Verios 460, FEI).

Supporting Information

Supporting Information is available from the Wiley Online Library or from the author.

Acknowledgements

This work was supported by NSF CBET-2034902 and Honda Research Institute USA, Inc. Set-up for all-solid-state-batteries was assisted by Dr. Sookyung Jeong.

Conflict of Interest

The authors declare no conflict of interest.

Data Availability Statement

The data that support the findings of this study are available in the supplementary material of this article.

Keywords

all-solid-state-battery, interlayer, lithium metal anode, mixed ionic and electronic conductor

Received: November 21, 2022

Revised: February 15, 2023

Published online:

- a) W. Li, E. M. Erickson, A. Manthiram, *Nat. Energy* **2020**, *5*, 26; b) J. Lu, Z. Chen, Z. Ma, F. Pan, L. A. Curtiss, K. Amine, *Nat. Nanotechnol.* **2016**, *11*, 1031; c) A. Fotouhi, D. J. Auger, K. Propp, S. Longo, M. Wild, *Renewable Sustainable Energy Rev.* **2016**, *56*, 1008.
- a) C. Niu, H. Lee, S. Chen, Q. Li, J. Du, W. Xu, J.-G. Zhang, M. S. Whittingham, J. Xiao, J. Liu, *Nat. Energy* **2019**, *4*, 551; b) J. Liu, Z. Bao, Y. Cui, E. J. Dufek, J. B. Goodenough, P. Khalifah, Q. Li, B. Y. Liaw, P. Liu, A. Manthiram, Y. S. Meng, V. R. Subramanian, M. F. Toney, V. V. Viswanathan, M. S. Whittingham, J. Xiao, W. Xu, J. Yang, X.-Q. Yang, J.-G. Zhang, *Nat. Energy* **2019**, *4*, 180; c) K. Yan, Z. Lu, H.-W. Lee, F. Xiong, P.-C. Hsu, Y. Li, J. Zhao, S. Chu, Y. Cui, *Nat. Energy* **2016**, *1*, 16010.
- a) R. Xu, X.-B. Cheng, C. Yan, X.-Q. Zhang, Y. Xiao, C.-Z. Zhao, J.-Q. Huang, Q. Zhang, *Mater* **2019**, *1*, 317; b) D. Lin, Y. Liu, Y. Cui, *Nat. Nanotechnol.* **2017**, *12*, 194.
- a) R. Gond, W. van Ekeren, R. Mogensen, A. J. Naylor, R. Younesi, *Mater. Horiz.* **2021**, *8*, 2913; b) K. Deng, Q. Zeng, D. Wang, Z. Liu, G. Wang, Z. Qiu, Y. Zhang, M. Xiao, Y. Meng, *Energy Storage Mater.* **2020**, *32*, 425.
- a) Y. Seino, K. Takada, B.-C. Kim, L. Zhang, N. Ohta, H. Wada, M. Osada, T. Sasaki, *Solid State Ionics* **2005**, *176*, 2389; b) C. Monroe, J. Newman, *J. Electrochem. Soc.* **2005**, *152*, A396; c) T. Sato, T. Morinaga, S. Marukane, T. Narutomi, T. Igarashi,

- Y. Kawano, K. Ohno, T. Fukuda, Y. Tsujii, *Adv. Mater.* **2011**, *23*, 4868; d) M. Baba, N. Kumagai, H. Fujita, K. Ohta, K. Nishidate, S. Komaba, B. Kaplan, H. Groult, D. Devilliers, *J. Power Sources* **2003**, *119–121*, 914; e) J. Wan, J. Xie, X. Kong, Z. Liu, K. Liu, F. Shi, A. Pei, H. Chen, W. Chen, J. Chen, X. Zhang, L. Zong, J. Wang, L. Q. Chen, J. Qin, Y. Cui, *Nat. Nanotechnol.* **2019**, *14*, 705; f) L. Xu, Y. Lu, C. Z. Zhao, H. Yuan, G. L. Zhu, L. P. Hou, Q. Zhang, J. Q. Huang, *Adv. Energy Mater.* **2020**, *11*, 2002360; g) D. H. S. Tan, A. Banerjee, Z. Chen, Y. S. Meng, *Nat. Nanotechnol.* **2020**, *15*, 170; h) D. H. S. Tan, A. Banerjee, Z. Deng, E. A. Wu, H. Nguyen, J.-M. Daux, X. Wang, J.-H. Cheng, S. P. Ong, Y. S. Meng, Z. Chen, *ACS Appl. Energy Mater.* **2019**, *2*, 6542.
- [6] a) M. Otoyama, M. Suyama, C. Hotehama, H. Kowada, Y. Takeda, K. Ito, A. Sakuda, M. Tatsumisago, A. Hayashi, *ACS Appl. Mater. Interfaces* **2021**, *13*, 5000; b) Y.-W. Byeon, H. Kim, *Electrochem* **2021**, *2*, 452; c) T. K. Schwietert, V. A. Arszewelska, C. Wang, C. Yu, A. Vasileiadis, N. J. J. De Klerk, J. Hageman, T. Hupfer, I. Kerkamm, Y. Xu, E. Van Der Maas, E. M. Kelder, S. Ganapathy, M. Wagemaker, *Nat. Mater.* **2020**, *19*, 428.
- [7] C. D. Fincher, D. Ojeda, Y. Zhang, G. M. Pharr, M. Pharr, *Acta Mater.* **2020**, *186*, 215.
- [8] B. Han, X. Li, Q. Wang, Y. Zou, G. Xu, Y. Cheng, Z. Zhang, Y. Zhao, Y. Deng, J. Li, M. Gu, *Adv. Mater.* **2022**, *34*, 2108252.
- [9] Y. Chen, Z. Wang, X. Li, X. Yao, C. Wang, Y. Li, W. Xue, D. Yu, S. Y. Kim, F. Yang, A. Kushima, G. Zhang, H. Huang, N. Wu, Y. W. Mai, J. B. Goodenough, J. Li, *Nature* **2020**, *578*, 251.
- [10] J. Zhang, C. Zheng, J. Lou, Y. Xia, C. Liang, H. Huang, Y. Gan, X. Tao, W. Zhang, *J. Power Sources* **2019**, *412*, 78.
- [11] a) H. J. Choi, D. W. Kang, J. W. Park, J. H. Park, Y. J. Lee, Y. C. Ha, S. M. Lee, S. Y. Yoon, B. G. Kim, *Adv. Sci.* **2022**, *9*, 2103826; b) A. L. Santhosha, L. Medenbach, J. R. Buchheim, P. Adelhelm, *Batteries Supercaps* **2019**, *2*, 524; c) S. W. Park, G. Oh, J. W. Park, Y. C. Ha, S. M. Lee, S. Y. Yoon, B. G. Kim, *Small* **2019**, *15*, 1900235.
- [12] a) L. Ye, X. Li, *Nature* **2021**, *593*, 218; b) N. Suzuki, N. Yashiro, S. Fujiki, R. Omoda, T. Shiratsuchi, T. Watanabe, Y. Aihara, *Adv. Energy Sustainability Res.* **2021**, *2*, 2100066; c) Y. Su, L. Ye, W. Fitzhugh, Y. Wang, E. Gil-González, I. Kim, X. Li, *Energy Environ. Sci.* **2020**, *13*, 908; d) F. J. Simon, M. Hanauer, F. H. Richter, J. Janek, *ACS Appl. Mater. Interfaces* **2020**, *12*, 11713; e) Y.-G. Lee, S. Fujiki, C. Jung, N. Suzuki, N. Yashiro, R. Omoda, D.-S. Ko, T. Shiratsuchi, T. Sugimoto, S. Ryu, J. H. Ku, T. Watanabe, Y. Park, Y. Aihara, D. Im, I. T. Han, *Nat. Energy* **2020**, *5*, 299; f) F. J. Simon, M. Hanauer, A. Henss, F. H. Richter, J. Janek, *ACS Appl. Mater. Interfaces* **2019**, *11*, 42186.
- [13] a) Q. Pan, D. M. Smith, H. Qi, S. Wang, C. Y. Li, *Adv. Mater.* **2015**, *27*, 5995; b) R. Mukherjee, A. V. Thomas, D. Datta, E. Singh, J. Li, O. Eksik, V. B. Shenoy, N. Koratkar, *Nat. Commun.* **2014**, *5*, 3710.
- [14] S. Y. Kim, J. Li, *Energy Mater. Adv.* **2021**, *2021*, 1519569.
- [15] a) T. Zhu, J. Li, *Prog. Mater. Sci.* **2010**, *55*, 710; b) H. J. Frost, M. F. Ashby, *Deformation Mechanism Maps: The Plasticity and Creep of Metals and Ceramics*, Pergamon Press, Oxford **1982**; c) L. Tian, J. Li, J. Sun, E. Ma, Z. W. Shan, *Sci. Rep.* **2013**, *3*, 2113.
- [16] J. Sung, N. Kim, J. Ma, J. H. Lee, S. H. Joo, T. Lee, S. Chae, M. Yoon, Y. Lee, J. Hwang, S. K. Kwak, J. Cho, *Nat. Energy* **2021**, *6*, 1164.
- [17] Y. An, Y. Tian, H. Wei, B. Xi, S. Xiong, J. Feng, Y. Qian, *Adv. Funct. Mater.* **2019**, *30*, 1908721.
- [18] a) S. Park, J. Sung, S. Chae, J. Hong, T. Lee, Y. Lee, H. Cha, S. Y. Kim, J. Cho, *ACS Nano* **2020**, *14*, 11548; b) J. Sung, J. Ma, S. H. Choi, J. Hong, N. Kim, S. Chae, Y. Son, S. Y. Kim, J. Cho, *Adv. Mater.* **2019**, *31*, 1900970.
- [19] a) Y. Son, J. Sung, Y. Son, J. Cho, *Curr. Opin. Electrochem.* **2017**, *6*, 77; b) J. Sung, N. Kim, S. P. Kim, T. Lee, M. Yoon, J. Cho, *Batteries Supercaps* **2022**, *5*, 202200136.
- [20] W. Guo, Z. Wang, J. Li, *Nano Lett.* **2015**, *15*, 6582.
- [21] A. M. K. Esawi, M. M. Farag, *Mater. Des.* **2007**, *28*, 2394.
- [22] Z. Liang, D. Lin, J. Zhao, Z. Lu, Y. Liu, C. Liu, Y. Lu, H. Wang, K. Yan, X. Tao, *Proc. Natl. Acad. Sci. U. S. A.* **2016**, *113*, 2862.
- [23] a) Y. Qi, L. G. Hector, C. James, K. J. Kim, *J. Electrochem. Soc.* **2014**, *161*, F3010; b) K. Li, H. Xie, J. Liu, Z. Ma, Y. Zhou, D. Xue, *Phys. Chem. Chem. Phys.* **2013**, *15*, 17658.

ADVANCED MATERIALS

Supporting Information

for *Adv. Mater.*, DOI: 10.1002/adma.202210835

Ultra-Thin Lithium Silicide Interlayer for Solid-State
Lithium-Metal Batteries

*Jaekyung Sung, So Yeon Kim, Avetik Harutyunyan,
Maedeh Amirmaleki, Yoonkwang Lee, Yeonguk Son, and
Ju Li**

Supporting information

Ultra-Thin Lithium Silicide Interlayer for Solid-State Lithium-Metal Batteries

*Jaekyung Sung, So Yeon Kim, Avetik Harutyunyan, Maedeh Amirmaleki, Yoonkwang Lee, Yeonguk Son, Ju Li**

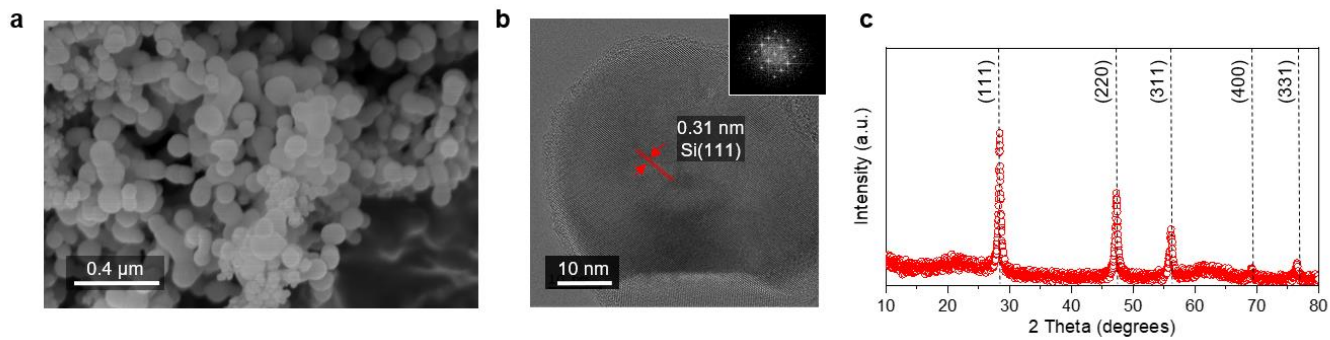


Figure S1. **a**, SEM images of SiNPs with the particle size of 50 nm. **b**, TEM images of single Si particle with d-spacing of 0.31 nm and inset showing a *Fast Fourier Transform*. **c**, XRD analysis of SiNPs.

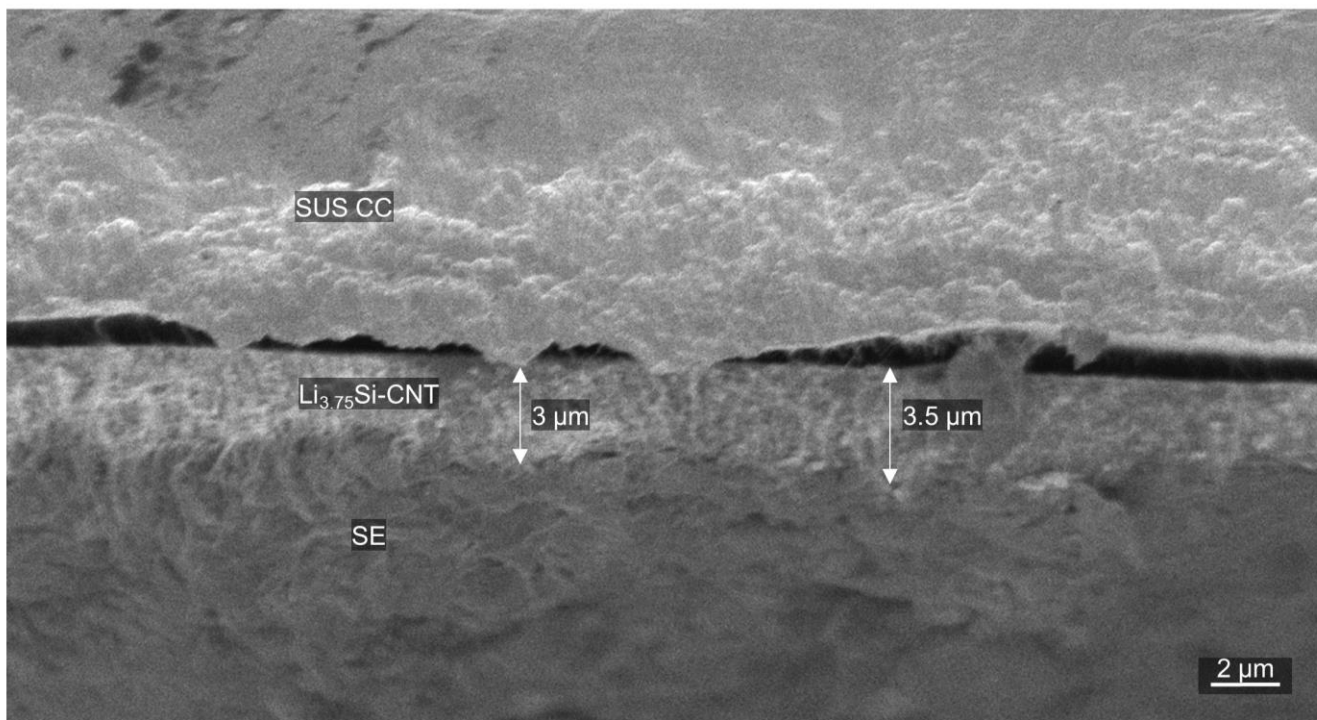


Figure S2. Magnified cross-sectional SEM images of $\text{Li}_{3.75}\text{Si-CNT}$ interlayer located between SE and a stainless-steel current collector (SUS CC).

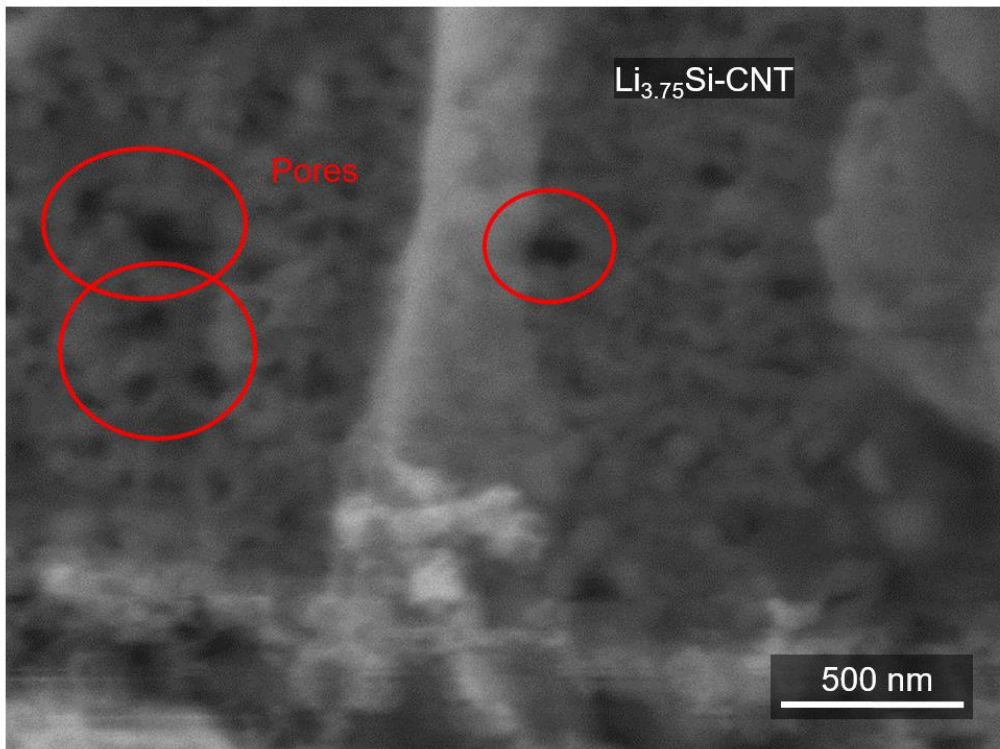


Figure S3. Cross-sectional SEM images of $\text{Li}_{3.75}\text{Si-CNT}$ layer cut by ion beam milling.

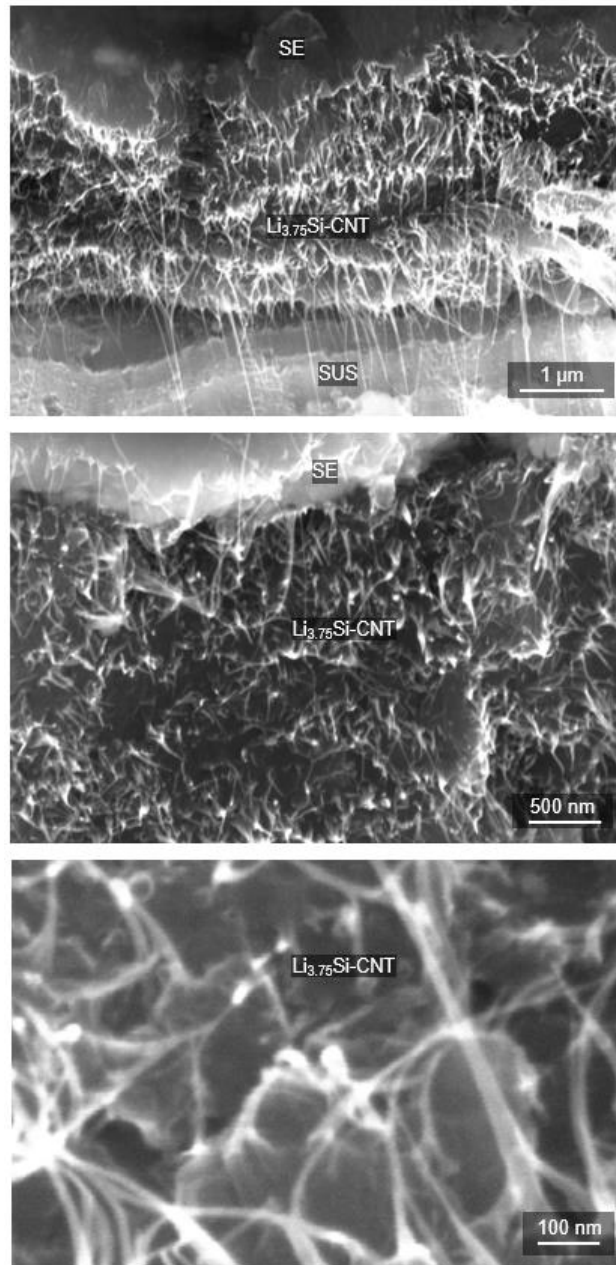


Figure S4. Cross-sectional SEM images of Li_{3.75}Si-CNT layer produced under stack pressure of 65 MPa. Cell configuration was SUS/Li_{3.75}Si-CNT/SE/Li_{BCC}.

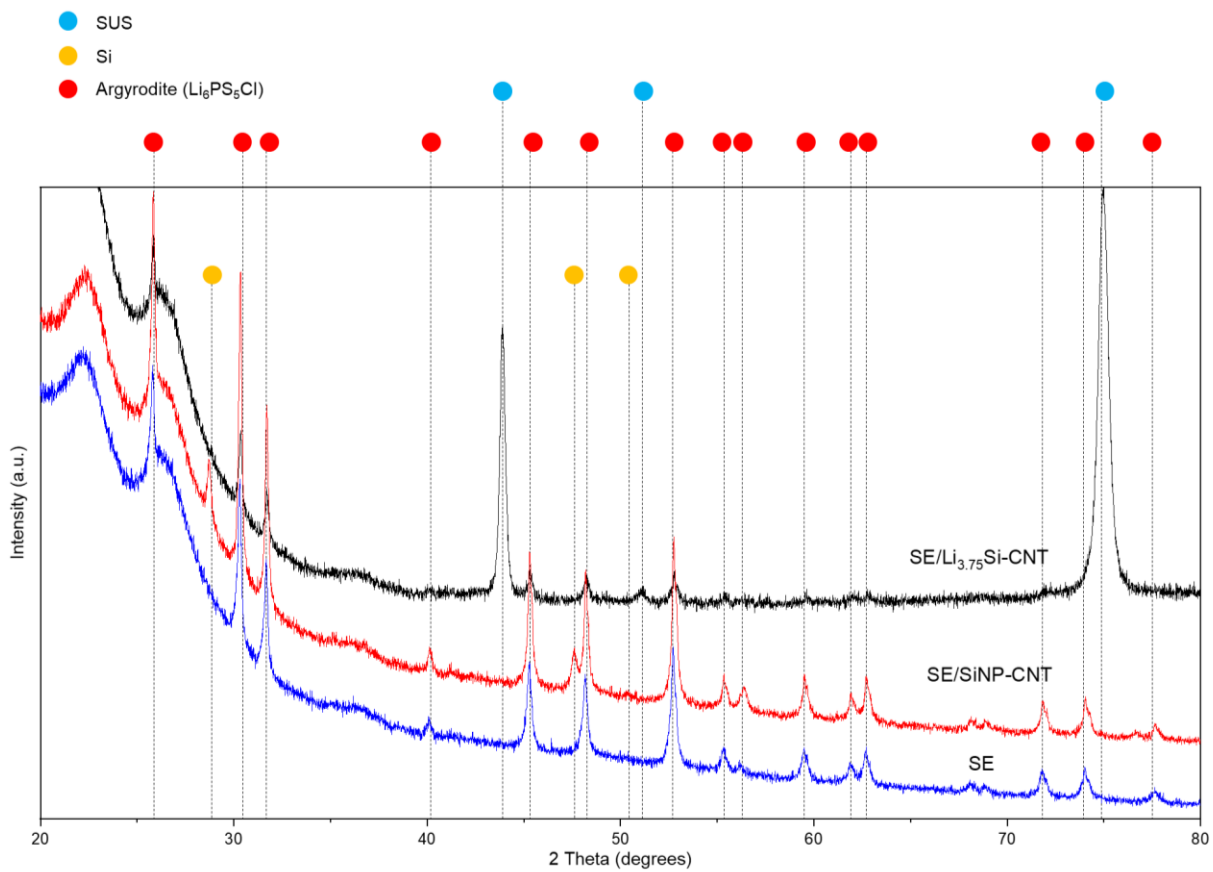


Figure S5. XRD analysis ($\text{Cu K}\alpha$ of wavelength 1.542 \AA) of SE ($\text{Li}_6\text{PS}_5\text{Cl}$), SE/SiNP-CNT, and SE/Li_{3.75}Si-CNT.

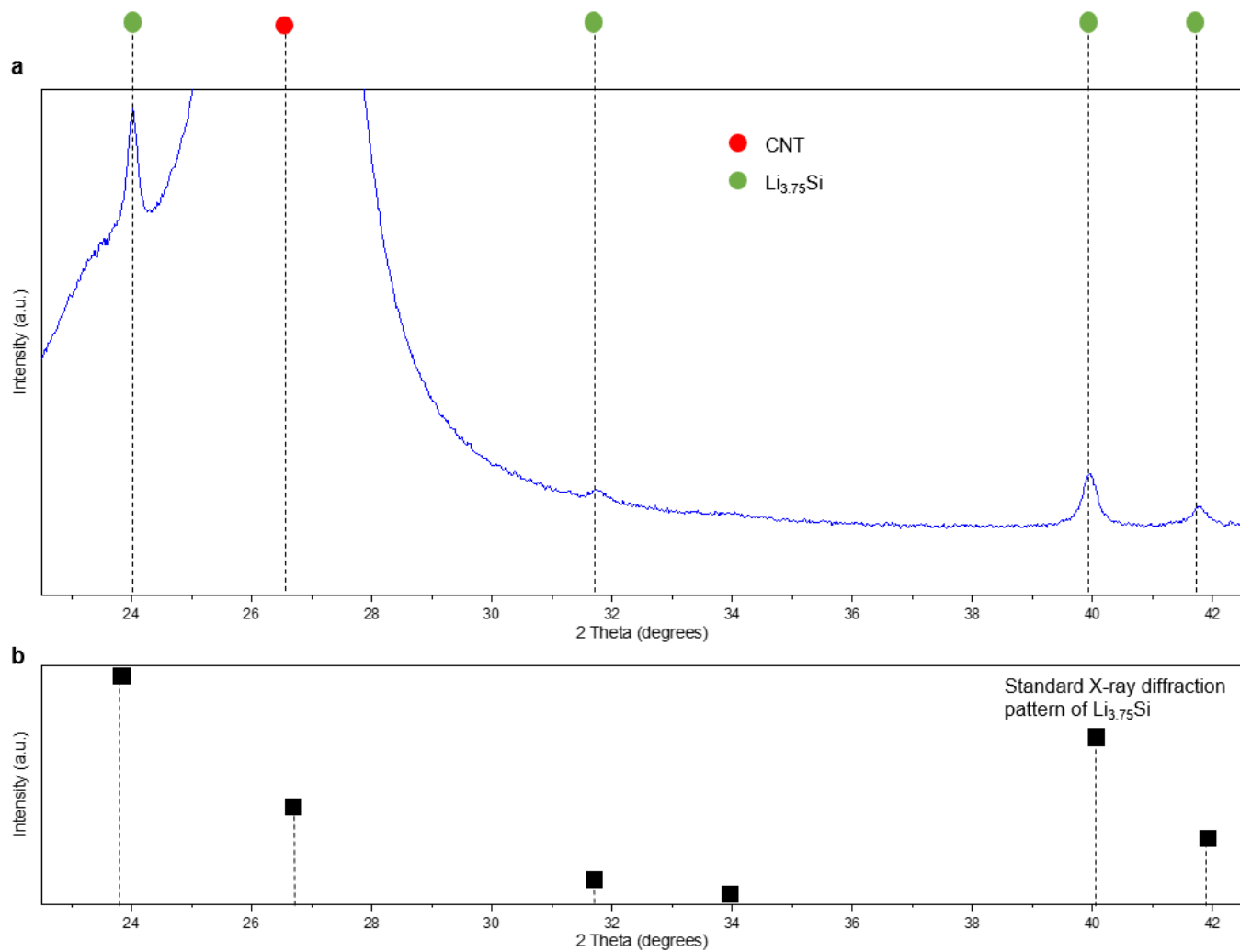


Figure S6. a, XRD analysis ($\text{Cu K}\alpha$ of wavelength 1.542 \AA) of $\text{Li}_{3.75}\text{Si}$ -CNT interlayer. **b**, Standard XRD pattern of $\text{Li}_{15}\text{Si}_4$ (mp-569849) from Material project powered by open-source software.

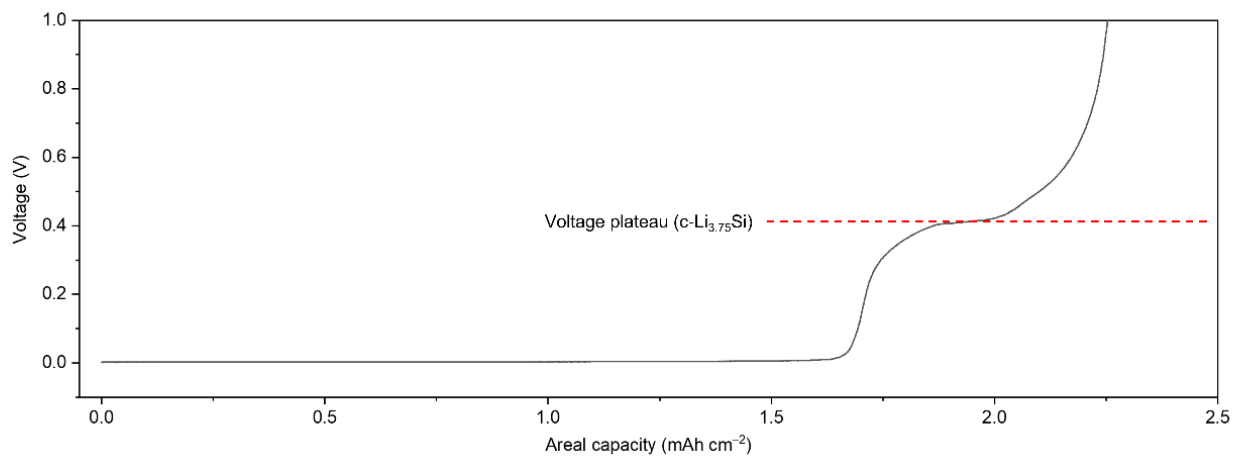


Figure S7. Voltage profile of $\text{Li}_{3.75}\text{Si-CNT}$ during discharging process (de-lithiation).

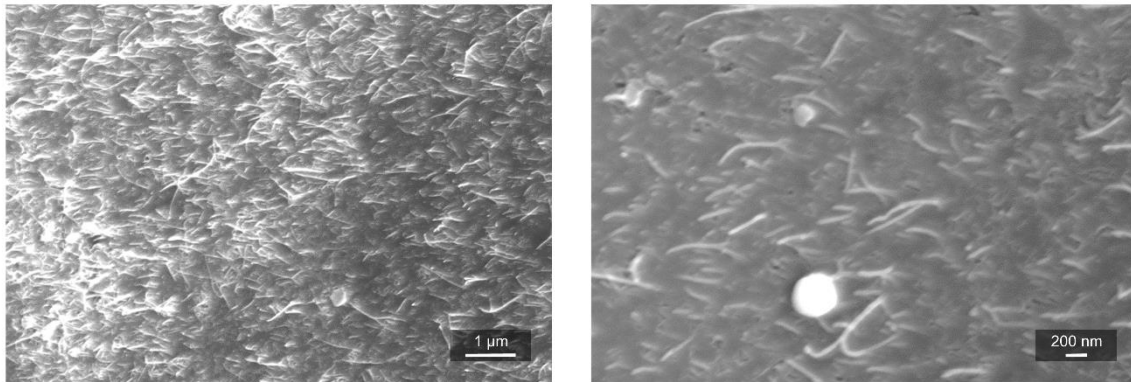


Figure S8. Top-view of SEM image of $\text{Li}_{3.75}\text{Si-CNT}$ surface after plating process (0.05 mAh cm^{-2})

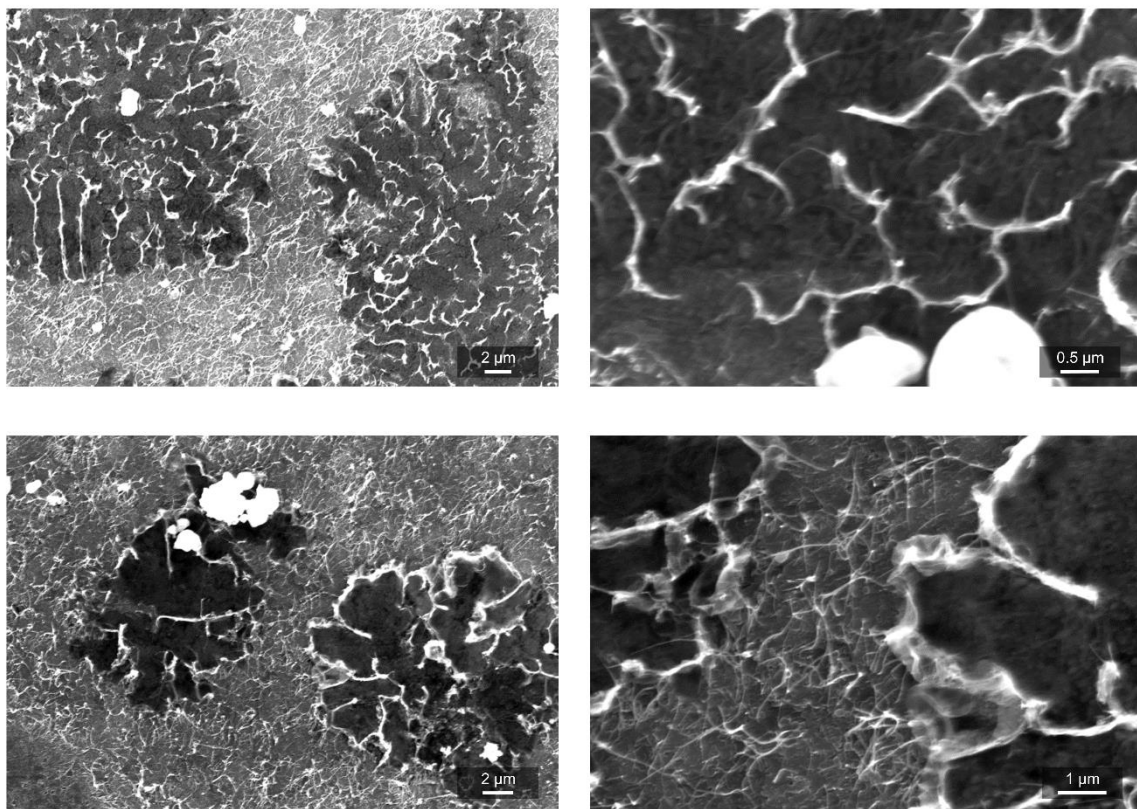


Figure S9. Top-view of SEM image of $\text{Li}_{3.75}\text{Si-CNT}$ surface after plating process (0.1 mAh cm^{-2})

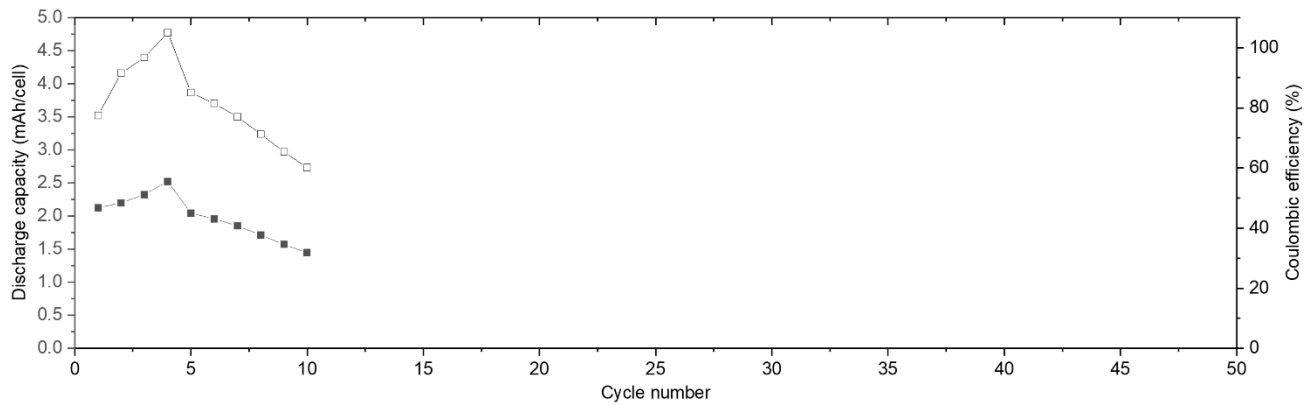


Figure S10. Discharge capacity retention of SUS/Li_{3.75}Si/SE/Li_{BCC}

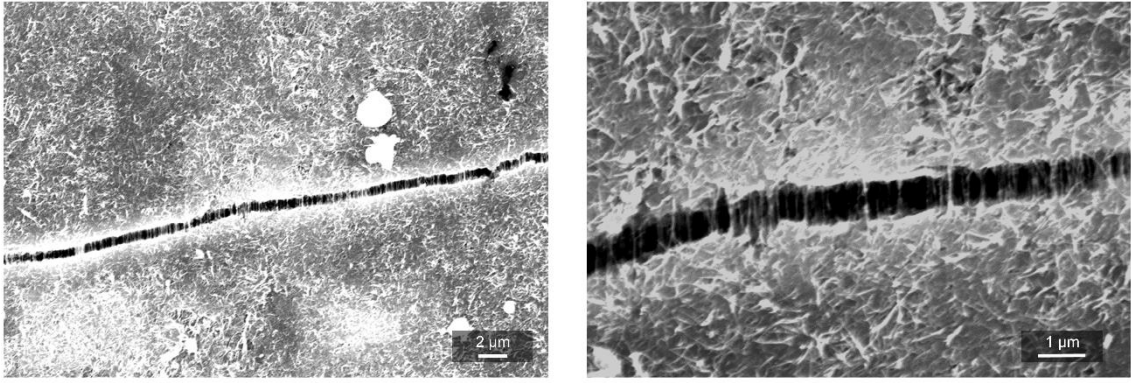


Figure S11. Top-view of SEM image of Li_{3.75}Si-CNT after stretching and bending electrode

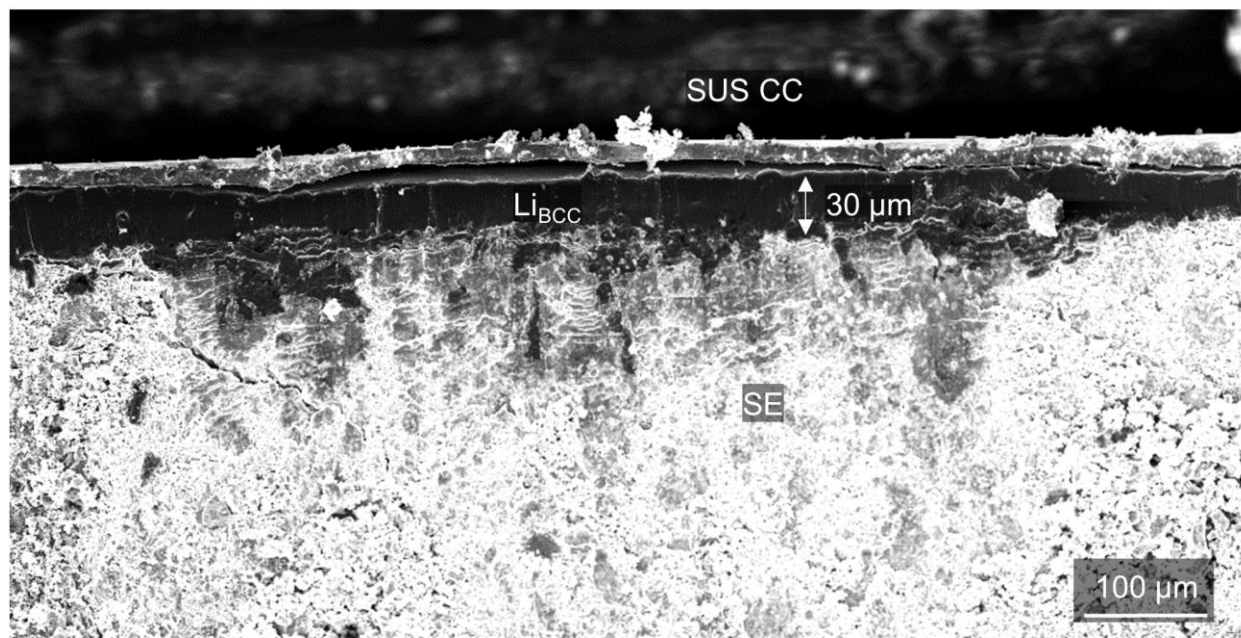


Figure S12. Cross-sectional SEM image showing the thickness of lithium foil (30 μm) in pristine Li_{BCC}/SiNP-CNT/SE/NCM811.

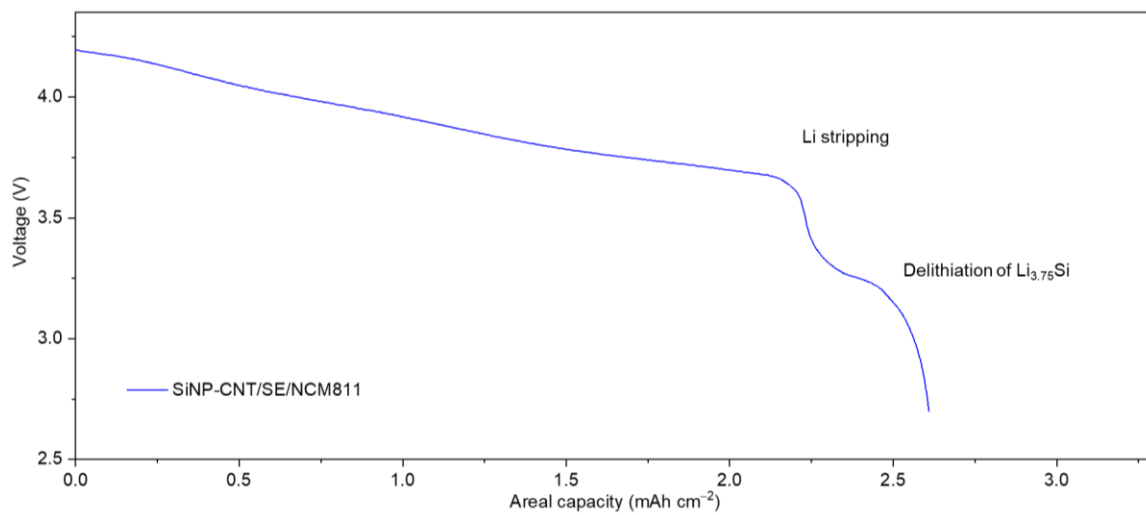


Figure S13. Discharge voltage profiles of SiNP-CNT/SE/NCM811 (e.g. there is no Li foil for non-electrochemical lithiation) clearly showing range of Li stripping and de-alloying reaction of Li_{3.75}Si at the first cycle.

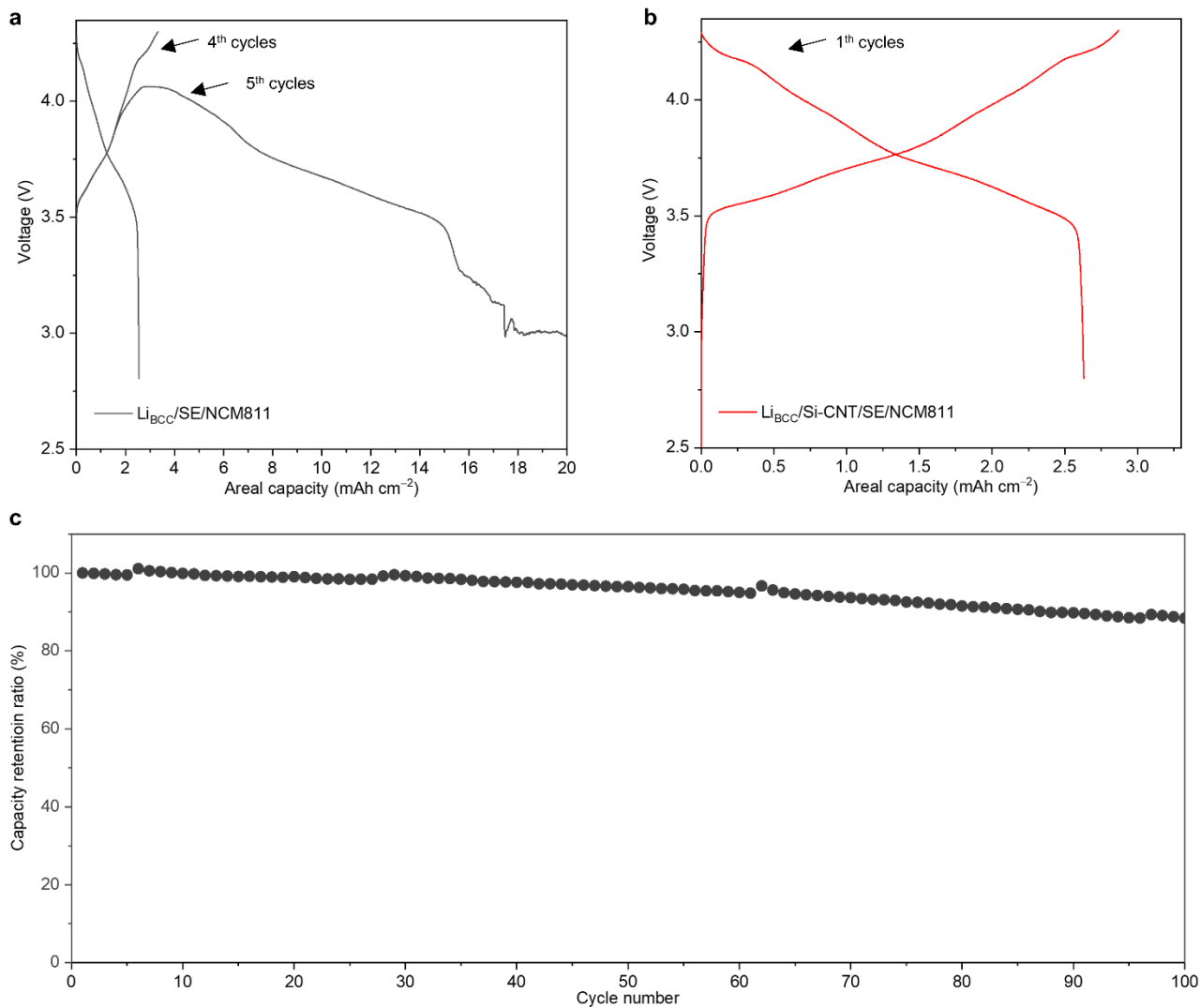


Figure S14. Voltage profiles of $\text{Li}_{\text{BCC}}/\text{SE}/\text{NCM811}$ (a) and $\text{Li}_{\text{BCC}}/\text{SiNP-CNT}/\text{SE}/\text{NCM811}$ (b) at stack pressure of 65 MPa and 5 MPa, respectively. (c) Capacity retention ratio of $\text{Li}_{\text{BCC}}/\text{Si-CNT}/\text{SE}/\text{NCM811}$ at stack pressure of 5 MPa.

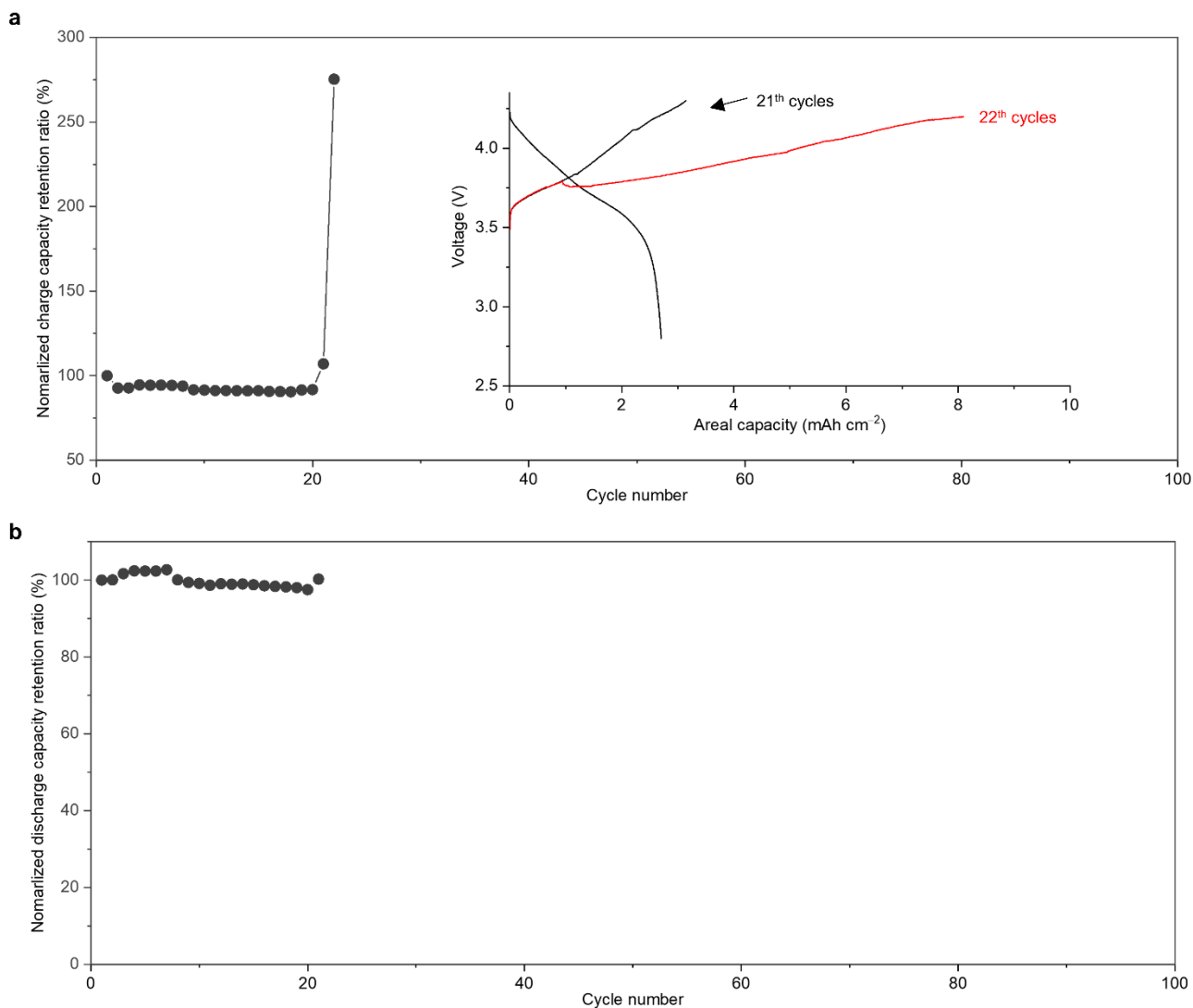


Figure S15. Normalized (a) charge and (b) discharge capacity retention of Li_{BCC}/SiNP-CNT/SE/NCM811 at stack pressure of 65 MPa and an inset showing voltage profile at 21 and 22th cycle. The stack pressure during the fabrication of the cell was 5 MPa and the cell was operated at stack pressure of 5 MPa for the first cycle.

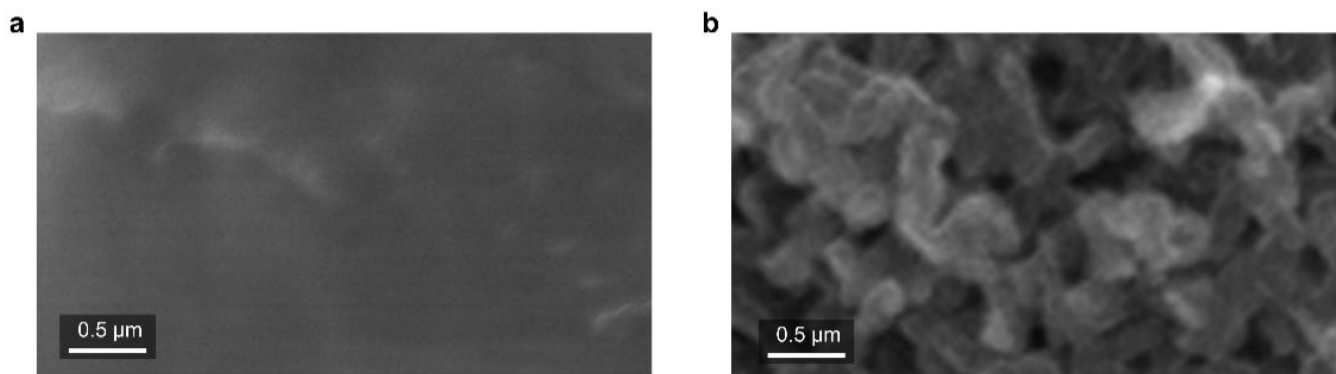


Figure S16. Cross-sectional SEM images of magnified lithium foil side in $\text{Li}_{\text{BCC}}/\text{SiNP-CNT}/\text{SE}/\text{NCM811}$ (a) after 200 cycles and $\text{Li}_{\text{BCC}}/\text{SE}/\text{NCM811}$ (b) after 73 cycles

Reference number	Interlayer	Interlayer thickness (μm)	Sort of the solid-electrolyte	Cell configuration	Type of cell	Full-cell			
						Initial Coulombic efficiency (%)	Rate capability (%) = Capacity at $x\text{C}/\text{capacity at } y\text{C}$	Sort of cathode	Capacity retention, % @cycle number /operating temperature
This work	LiSi-CNT	3.25	LPSCI	Half-cell Full-cell	Swagelok	92.0	76% (5C/0.05C)	$\text{LiNi}_{0.80}\text{Co}_{0.10}\text{Mn}_{0.10}\text{O}_2$	97.65% @49 cycles /25 °C 88.9% @200 cycles /60 °C
1	Indium	125	Li3PS4	Symmetric cell	Swagelok	-	-	-	-
2	Silver	10	LPSCI	Full-cell	Homemade pressurized cell	~88%	69.5% (6C/0.2C)	$\text{LiNi}_{0.60}\text{Co}_{0.20}\text{Mn}_{0.20}\text{O}_2$	94.3% @140 cycles /55 °C
3	Graphite	30–35	LGPS	Symmetric cell Full-cell	Homemade pressurized cell	91.4	-	LiCoO_2	~90% @100 cycles /35 °C
4	Silver-carbon composites	10	LPSCI	Full-cell	Pouch	-	> 80% (2C/0.2C)	$\text{LiNi}_{0.90}\text{Co}_{0.05}\text{Mn}_{0.05}\text{O}_2$	89% @1000 cycles /60 °C
5	Zinc-carbon	10	LPSCI	Full-cell	Pouch	-	~87%	$\text{LiNi}_{0.90}\text{Co}_{0.05}\text{Mn}_{0.05}\text{O}_2$	~50% @300

	composites						(1C/0.1C)	O ₂	cycles /60 °C
5	Aluminum-carbon composites	10	LPSCI	Full-cell	Pouch	-	~78% (1C/0.1C)	LiNi _{0.90} Co _{0.05} Mn _{0.05} O ₂	~70% @300 cycles /60 °C
5	Tin-carbon composites	10	LPSCI	Full-cell	Pouch	-	~73% (1C/0.1C)	LiNi _{0.90} Co _{0.05} Mn _{0.05} O ₂	~68% @300 cycles /60 °C
5	Nickel-carbon composites	10	LPSCI	Full-cell	Pouch	-	~92% (1C/0.1C)	LiNi _{0.90} Co _{0.05} Mn _{0.05} O ₂	-
6	PEO10:LiTF SI	50 - 200	LPSCI	Symmetric cell	Swagelok	-	-	-	-
7	PEO20:LiTF SI	20	LPSCI	Symmetric cell	Swagelok	-	-	-	-
8	Magnesium	0.005~0.1	Li ₇ La ₃ Zr ₂ O ₁₂	Symmetric cell	Coin	-			
9	Co ₃ O ₄	~ 0.1	Li _{6.5} La ₃ Zr _{1.5} Ta _{0.5} O ₁₂	Symmetric cell	Coin	-			
10	Ag/LiF	0.2	Li _{6.4} La ₃ Zr _{1.4} Ta _{0.6} O ₁₂	Symmetric cell Full-cell	Coin		~86% (5C/0.2C)	LFP	~90% @260 0 cycles / 60°C

Table S1. Comparison of the previously proposed interlayers and LiSi-CNT interlayer for all-solid-state-battery using lithium anode.

Table S2. Various parameters for porosity calculation of SiNP-CNT and Li_{3.75}Si-CNT

Porosity of SiNP-CNT			Porosity of Li _{3.75} Si-CNT		
True density of carbon	2.1	g/cc	True density of carbon	2.1	g/cc
Weight of carbon	0.000015	g	Weight of carbon	0.000015	g
Total volume of carbon	7.14286E-06	cc	Total volume of carbon	7.14286E-06	cc
True density of Si	2.33	g/cc	True density of Li _{3.75} Si	1.22	g/cc
Weight of Si	0.000135	g	Weight of Li _{3.75} Si (90%)	0.000260114	g
Total volume of Si	5.79399E-05	cc	Total volume of Li _{3.75} Si	0.000213208	cc
			Total volume of carbon	1.37626E-05	
Thickness of electrode	0.0002	cm	Thickness of Li _{3.75} Si	0.000325	cm
Area of electrode	0.785	cm ²	Area of Li _{3.75} Si	0.785	cm ²
Total volume of electrode	0.000157	cc	Total volume of electrode	0.000255125	cc
Volume ratio of Si MIEC	41.45399446	%	Volume ratio of Li _{3.75} Si	88.96446595	%
Porosity	58.54600554	%	Porosity	11.03553405	%

Reference

- [1] A. L. Santhosha, L. Medenbach, J. R. Buchheim, P. Adelhelm, *Batter. Supercaps* **2019**, 2, 524.
- [2] H. J. Choi, D. W. Kang, J. W. Park, J. H. Park, Y. J. Lee, Y. C. Ha, S. M. Lee, S. Y. Yoon, B. G. Kim, *Adv. Sci. (Weinh)* **2022**, 9, e2103826.
- [3] Y. Su, L. Ye, W. Fitzhugh, Y. Wang, E. Gil-González, I. Kim, X. Li, *Energy Environ. Sci.* **2020**, 13, 908.
- [4] Y.-G. Lee, S. Fujiki, C. Jung, N. Suzuki, N. Yashiro, R. Omoda, D.-S. Ko, T. Shiratsuchi, T. Sugimoto, S. Ryu, J. H. Ku, T. Watanabe, Y. Park, Y. Aihara, D. Im, I. T. Han, *Nat. Energy* **2020**, 5, 299.
- [5] N. Suzuki, N. Yashiro, S. Fujiki, R. Omoda, T. Shiratsuchi, T. Watanabe, Y. Aihara, *Adv. Energy Sustainability Res.* **2021**.
- [6] F. J. Simon, M. Hanauer, A. Henss, F. H. Richter, J. Janek, *ACS Appl. Mater. Interfaces* **2019**, 11, 42186.
- [7] F. J. Simon, M. Hanauer, F. H. Richter, J. Janek, *ACS Appl. Mater. Interfaces* **2020**, 12, 11713.
- [8] K. K. Fu, Y. Gong, Z. Fu, H. Xie, Y. Yao, B. Liu, M. Carter, E. Wachsman, L. Hu, *Angew. Chem.* **2017**, 56, 14942.
- [9] X. He, S. Hua, F. Yan, H. Bai, B. Shen, J. Zhai, *Chem. Eng. J.* **2021**, 421.
- [10] S. Lee, K.-s. Lee, S. Kim, K. Yoon, S. Han, M. H. Lee, Y. Ko, J. H. Noh, W. Kim, K. Kang, *Sci. Adv.* **2022**, 8, eabq0153.